

# Template-Based Fabrication of Porous Carbon for High-Performance Supercapacitor Electrode

Jiayi Chen, Yongda Cao, Dongjia Xie, Jingrui Wang, Xiao Wu, Yangsong Tang, and Yuan Wang\*

Porous carbon materials attract substantial research interest as promising electrode materials for supercapacitors, owing to their high specific surface area, excellent electrical conductivity, and remarkable chemical and thermal stability. Diverse synthesis strategies have been explored to improve the electrochemical performance of porous carbon electrodes. Among these, the template method demonstrates significant potential for precisely constructing porous architectures, showing great promise for both probing energy storage mechanisms and fabricating high-performance carbon materials. This review comprehensively examines sacrificial templating strategies for synthesizing porous

carbon materials, beginning with an overview of the design principles for hierarchical porous architectures. The templating methods are classified into three main categories—hard, soft, and self-templating—with a discussion of their respective formation mechanisms and recent methodological advances. The influence of these strategies on the morphological, structural, and electrochemical properties of the resulting carbons is analyzed. Finally, current challenges and future research directions are outlined to facilitate the application of templated porous carbons in high-performance supercapacitors.

## 1. Introduction

As fossil fuel reserves dwindle and the environmental pollution arising from their combustion intensifies, the development of sustainable and high-performance energy conversion and storage technologies has become an urgent priority.<sup>[1]</sup> The energy storage landscape encompasses a variety of devices, such as supercapacitors,<sup>[2,3]</sup> hybrid capacitors (e.g., Zn-ion based<sup>[4,5]</sup>), and batteries (e.g., hybrid-ion,<sup>[6]</sup> Zn-air,<sup>[7]</sup> ammonium-ion<sup>[8,9]</sup>), alongside advanced materials like single-atom catalysts<sup>[10]</sup> that are pivotal to enhancing their performance. Among these various energy-storage devices, supercapacitors stand out owing to their exceptional power density, rapid charge–discharge kinetics, outstanding cycling stability, broad operating-temperature range, and environmentally benign nature.<sup>[11,12]</sup> These characteristics render supercapacitors particularly well suited to address the pressing demand for efficient, fast-response energy-storage systems.

According to their underlying storage mechanisms, supercapacitors can be broadly categorized into electric double-layer capacitors (EDLCs) and pseudocapacitors.<sup>[13]</sup> EDLCs store charge reversibly by physical adsorption and desorption of electrolyte ions at the electrode–electrolyte interface, forming an electric double layer without involving Faradaic reactions; this endows them with exceptionally high power density and outstanding cycling stability.<sup>[14,15]</sup> In contrast, pseudocapacitors rely on fast, reversible Faradaic redox processes at the electrode surface, complemented by surface-confined pseudocapacitive behavior and near-surface ion adsorption/desorption, allowing for higher energy densities within a limited voltage window, albeit with somewhat reduced power response and cycle life compared to EDLCs.<sup>[16–18]</sup> Consequently, the choice of electrode material is critical to supercapacitor performance. Owing to their large specific surface area, excellent electrical conductivity, and robust chemical and thermal stability, porous carbon materials provide abundant sites for ion adsorption and support efficient electron transport, making them the electrode material of choice.

To develop porous carbon materials that deliver both outstanding electrochemical performance and cost-effectiveness without compromising high-power capability, several synthetic approaches have been explored, including direct pyrolysis,<sup>[19–21]</sup> physical or chemical activation,<sup>[22,23]</sup> and templating techniques.<sup>[24–26]</sup> Direct pyrolysis typically yields carbons with limited porosity, while conventional activation methods, though effective at creating high surface areas and microporosity as seen in biochar adsorbents,<sup>[27,28]</sup> often lack the precision needed to construct the well-defined hierarchical pore architectures essential for advanced electrochemical applications. It is precisely this need for precise control that makes templating techniques particularly attractive, particularly since they 1) faithfully replicate

J. Chen, D. Xie, J. Wang, X. Wu, Y. Wang  
School of Chemical Engineering  
Sichuan University  
Chengdu 610065, China  
E-mail: wangyuan2022@scu.edu.cn

Y. Cao  
Natural Gas Research Institute  
PetroChina Southwest Oil & Gasfield Company  
Chendu 610213, China  
  
Y. Tang  
State Grid Sichuan Electric Power Company  
Yingxiawan Hydropower Station  
Chengdu 610072, China

the template's architecture, ensuring uniform pore size, morphology, and inter-pore spacing; 2) offer highly tunable parameters, such as template type, dimensions, carbonization temperature, and dwell time, to optimize pore characteristics; 3) accommodate a wide range of precursors, from various organic polymers to inorganic carbon sources or biomass; 4) readily produce three-dimensionally interconnected pore networks that facilitate electrolyte infiltration and rapid ion transport; and 5) are relatively mature and scalable, allowing batch production with existing industrial equipment. Consequently, templating has emerged as an ideal route for fabricating high-performance porous carbon electrodes.

In the templated synthesis of porous carbons, the carbon precursor is first homogeneously combined with the chosen template and then subjected to high-temperature pyrolysis, during which the template serves as a rigid scaffold to preserve the pore architecture. Following carbonization, the template is typically removed via chemical etching or solvent extraction, yielding an ordered pore network that mirrors the template's original geometry. Templates can be classified into three main categories based on their nature: 1) hard templates, such as

silica or metal oxides that furnish a robust framework for well-defined meso- and macropores;<sup>[29]</sup> 2) soft templates, which include small organic molecules, surfactants, or block copolymers, exhibit self-assembly behavior that directs the formation of tunable nanoscale porosity<sup>[30]</sup>; and 3) self-templates, a category encompassing biomass and metal-organic frameworks (MOFs), utilize the precursor's intrinsic structure to induce pore formation, thereby eliminating the need for an external template.<sup>[31]</sup> Each of these templating strategies offers unique advantages, providing versatile routes to engineer porous carbon electrodes with precisely controlled architectures and superior electrochemical performance.

Although numerous reviews have explored synthetic strategies for porous carbons in supercapacitors, a dedicated discussion on templating methods is less common. This review provides a focused analysis of hard, soft, and self-templating strategies, examining their mechanisms, advances, and influence on electrochemical performance, as shown in **Figure 1**. Current challenges and future research directions are also outlined to guide the design of high-performance porous carbon electrodes.



**Jiayi Chen** is currently pursuing a degree in Chemical Engineering and Technology at the School of Chemical Engineering, Sichuan University. Her research focuses on supercapacitors and electrochemistry.



**Yongda Cao** is an engineer at the Research Institute of Natural Gas Technology, PetroChina Southwest Oil & Gasfield Company. Her research focuses on CCUS and electrochemical energy storage.



**Dongjia Xie** is currently pursuing a master's degree in Chemical Engineering at the College of Chemical Engineering, Sichuan University. His research focuses on the preparation and modification of perovskite solar cells.



**Jingrui Wang** is studying for a bachelor's degree at the School of Chemical Engineering, Sichuan University, starting from 2024. He is under the guidance of Supervisor Wang Yuan. His current research interests focus on supercapacitors and their electrode materials.



**Xiao Wu** is a student in the Department of Process Equipment and Control Engineering, School of Chemical Engineering, Sichuan University. His research focuses on electrochemistry.



**Yangsong Tang** obtained his Bachelor's degree in Water Resources and Hydropower Engineering from Sichuan Agricultural University in 2014, and a Master's degree in Control Engineering from Wuhan University in 2019. He currently works at the State Grid Sichuan Yingxiawan Hydropower Plant, primarily engaged in hydropower production and related technical work.



**Yuan Wang** obtained his Ph.D. from the School of Chemical Engineering at Sichuan University. He is currently working as a postdoctoral researcher at Sichuan University, with a primary research focus on electrode design, electrocatalysis, and aqueous energy storage batteries.

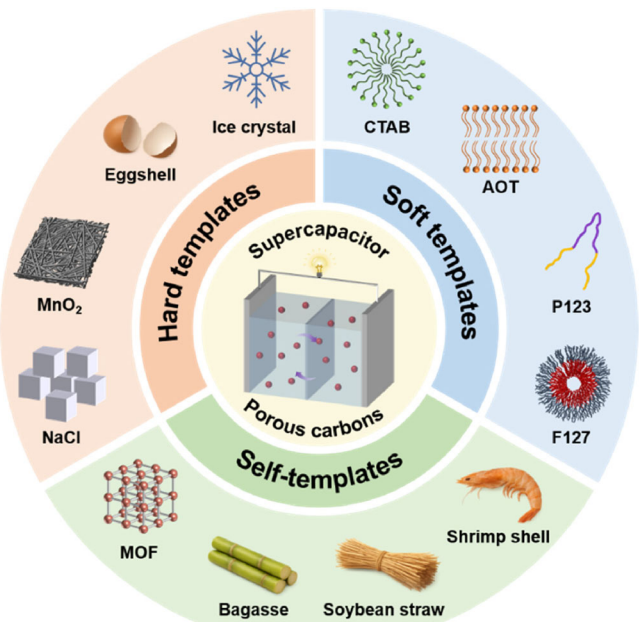


Figure 1. Schematic diagram of diverse template strategies for constructing HPCs used in supercapacitor electrodes.

## 2. Hierarchical Pore Architecture Design

In porous carbon electrodes, micropores (<2 nm), mesopores (2–50 nm), and macropores (>50 nm) coexist, each contributing complementary functions.<sup>[32]</sup> Micropores, by virtue of their ultra-high specific surface area, facilitate electric double-layer formation at the carbon-electrolyte interface and thereby furnish abundant reversible adsorption sites for charge storage; an increased fraction of microporosity directly enhances the electrode's energy density.<sup>[33]</sup> Mesopores serve as rapid ion-transport highways, markedly reducing diffusion resistance and consequently improving both power density and rate capability.<sup>[34]</sup> Macropores function as electrolyte reservoirs and buffer zones, quickly supplying ions during high-rate charge-discharge cycles to mitigate concentration polarization, sustain high power output, and bolster cycling stability.<sup>[35]</sup> In practice, macropores first store and buffer the electrolyte before releasing ions into the mesopore network, which in turn directs ions with minimal

resistance toward the microporous regions where charge is stored<sup>[36,37]</sup> (Figure 2). An optimal hierarchical pore architecture therefore requires a carefully balanced spatial distribution of micropores, mesopores, and macropores; their synergistic interplay not only accelerates ion transport but also enables simultaneous attainment of high energy density, enhanced power performance, and improved long-term stability.

To realize precise construction of the hierarchical pore architecture described above, templating methods play a central role by controlling the template size, morphology and loading.<sup>[38]</sup> Templates directly reproduce target pore sizes according to their own dimensions: coarse particulate metal oxides or water-soluble salts yield macropores, colloidal SiO<sub>2</sub> nanoparticles or emulsion templates form mesopores, and MOFs or polymeric templates that decompose/volatilize during heat treatment generate micropores. Beyond size, the template's morphology, dosage and the method used for template removal critically influence the pore-volume distribution and interconnectivity at each scale.<sup>[39]</sup> Common strategies include precise tuning of a single template, combining templates of different length scales, and coupling templating with chemical or physical activation (where activation further etches microporosity), thereby enabling synergistic optimization of micro/meso/macropores. In summary, judicious selection and combination of template systems together with appropriate activation and post-treatment are essential for constructing efficient hierarchical porous carbon (HPC) electrodes and ultimately achieving high-performance supercapacitors.

## 3. Template Methods

In templated syntheses of porous carbon materials, commonly used templates are classified into three types: hard templates, soft templates, and self-templates.<sup>[40,41]</sup> Hard templates (e.g., metal oxides, soluble salts) exhibit strong structural and thermal stability and therefore can accurately replicate pore architectures, but their removal typically requires harsh chemical treatments (strong acids or bases), making the process relatively cumbersome.<sup>[42]</sup> Soft templates (e.g., surfactants, block copolymers) readily self-assemble into ordered pore structures and are operationally simpler; however, their poor thermal stability during carbonization can lead to pore collapse.<sup>[43,44]</sup>

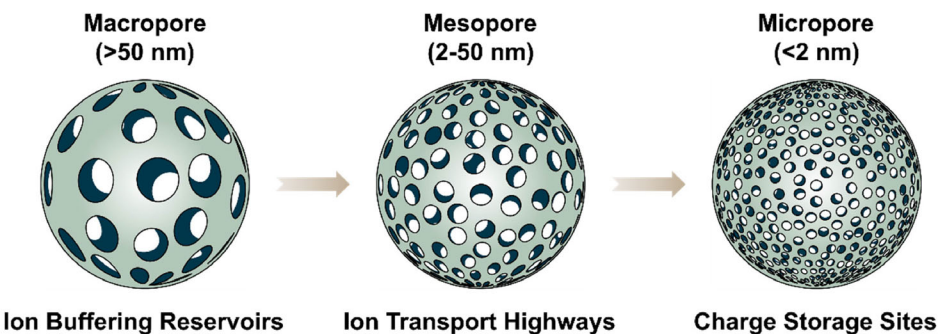


Figure 2. Schematic diagram illustrating the complementary functions of macro-, meso-, and micropores in HPC electrodes for supercapacitors.

Self-templates (e.g., MOFs, biomass) obviate the need for external template addition and removal and thus enable more efficient processing, yet the resulting pore architecture is highly dependent on precursor properties and is relatively difficult to control.<sup>[45]</sup> Consequently, selecting an appropriate templating agent is crucial for the precise tuning of porous carbon pore architecture and for optimizing their performance in supercapacitor applications.

### 3.1. Hard Templates

Hard-template methods are among the most effective approaches for synthesizing porous carbon materials with precisely controlled hierarchical pore structures.<sup>[46]</sup> Hard templates such as ZnO,<sup>[47–49]</sup> MgO,<sup>[50,51]</sup> NaCl,<sup>[52–54]</sup> KCl,<sup>[55,56]</sup> SiO<sub>2</sub>,<sup>[57–62]</sup> and PVB<sup>[63]</sup> are commonly employed to produce porous carbon. The hard-template preparation of porous carbon generally comprises four main steps: 1) preparation of the desired hard template; 2) homogeneous mixing of the carbon precursor with the hard template; 3) high-temperature carbonization under an inert atmosphere; and 4) removal of the template by chemical etching.<sup>[64,65]</sup>

#### 3.1.1. Metal Oxide Templates

Metal oxides, owing to their excellent thermal stability, are able to maintain their original morphology without reacting with the carbon precursor during high-temperature carbonization, thereby enabling the porous carbon to faithfully replicate the size and shape of the oxide template. Zhang et al. employed MnO<sub>2</sub> nanowires as templates and selected aniline and phytic acid as the carbon precursor and N/P sources. After coating the precursors onto the MnO<sub>2</sub> nanowires, carbonization and template removal yielded N/P codoped porous carbon (NPPCs). The study showed that the carbonization temperature strongly influenced the pore

structure and electrochemical performance; the sample carbonized at 700 °C (NPPC-700, surface area 142.97 m<sup>2</sup> g<sup>-1</sup>) exhibited the best performance, delivering a volumetric capacitance of 398.11 F cm<sup>-3</sup> at 0.5 A g<sup>-1</sup> and retaining 93.12% of its capacitance after 10,000 cycles at 5 A g<sup>-1</sup>.<sup>[66]</sup> (Figure 3). Zhang et al. also used MgO cubes as templates, with waste-tire pyrolysis oil (WTPO) serving as the carbon source and sulfur/nitrogen dopant. The resulting porous carbon (CHPC) combined abundant micro/mesoporosity with moderate S/N codoping and inherited the cubic morphology of the MgO template after template removal. The material exhibited a Brunauer-Emmett-Teller (BET) surface area of 1190 m<sup>2</sup> g<sup>-1</sup>. A symmetric capacitor assembled from this material (CHPC-2/CHPC-2; single-electrode loading 2 mg cm<sup>-2</sup>) showed a specific capacitance of 199.0 F g<sup>-1</sup> at 1 A g<sup>-1</sup> and retained 98.5% of its capacitance after 20,000 rapid charge-discharge cycles at 6 A g<sup>-1</sup>.<sup>[51]</sup> Wang et al. employed ZnO nanoparticles as templates to produce an N/P-codoped hierarchical porous carbon (NP-HPC) with a BET surface area of 999.66 m<sup>2</sup> g<sup>-1</sup>. When used as electrode material for supercapacitors, NP-HPC-2 delivered a specific capacitance of 394.51 F g<sup>-1</sup> at 0.2 A g<sup>-1</sup> and still retained 200.21 F g<sup>-1</sup> even at an ultrahigh current density of 50 A g<sup>-1</sup>, indicating excellent rate capability. Moreover, NP-HPC-2 maintained 95.7% of its initial capacitance after 10,000 cycles at 5 A g<sup>-1</sup>.<sup>[67]</sup> Ni et al. prepared a series of porous carbons using nanoAl<sub>2</sub>O<sub>3</sub> as the template; the best sample, BTC-0.2-2-800, combined rich porosity with a high oxygen content and exhibited a BET surface area of 1713.1 m<sup>2</sup> g<sup>-1</sup>. As an EDLC electrode, BTC-0.2-2-800 showed low resistance and outstanding rate performance, with a specific capacitance of 292.1 F g<sup>-1</sup> at 1 A g<sup>-1</sup> and 221.7 F g<sup>-1</sup> at 20 A g<sup>-1</sup>. In terms of cycling stability, no significant capacitance decay was observed after 10,000 continuous charge-discharge cycles at 10 A g<sup>-1</sup>.<sup>[68]</sup> Zhang et al. using microwave-assisted heating and CaO as the template, prepared naturally N-doped hierarchical porous carbon (NNHPC) from kapok and Chlorella. In this system, CaO both enlarged pore channels and, via active sites, promoted tar cracking into smaller molecules,

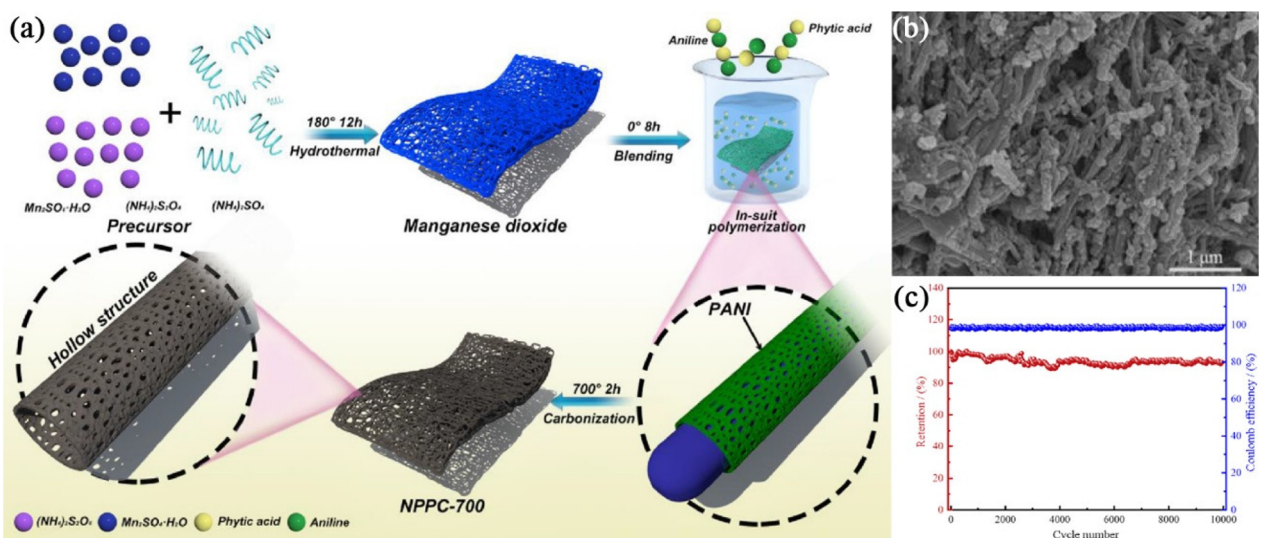


**Figure 3.** a) Schematic illustration for the preparation of NPPCs. b) Scanning electron microscope (SEM) images and c) cycling stability and Coulomb efficiency of NPPC-700 (Reproduced from ref. [66] with permission from Elsevier).

thereby reducing tar deposition within the pores, while also inhibiting complete decomposition of proteinaceous nitrogen and favoring the retention of N-containing compounds in the char. The optimal sample, NNHPC-1CaO, achieved a BET surface area of  $3117.73 \text{ m}^2 \text{ g}^{-1}$  and a micropore volume of  $0.71 \text{ cm}^3 \text{ g}^{-1}$ . Electrochemically, NNHPC-1CaO exhibited a specific capacitance of  $429.18 \text{ F g}^{-1}$  at  $0.2 \text{ A g}^{-1}$ , and a button-type cell assembled from this material retained 99.51% of its capacitance after 10,000 cycles at  $10 \text{ A g}^{-1}$ <sup>[69]</sup>. Our previous work used ZnO as a sacrificial template to prepare nitrogen-doped porous carbon fibers NPCF on carbon fibers. After impregnating the NPCF with bismuth nitrate and performing low-temperature pyrolysis, we obtained a  $\text{Bi}_2\text{O}_3$ @NPCF composite electrode. Electrochemical characterization in 2 M KOH electrolyte at a current density of  $1 \text{ mA cm}^{-2}$  showed areal capacitances of  $1163.0 \text{ mF cm}^{-2}$  for NPCF and  $1034.8 \text{ mF cm}^{-2}$  for  $\text{Bi}_2\text{O}_3$ @NPCF. In 2 M NaOH the

areal capacitances were  $453.9 \text{ mF cm}^{-2}$  for NPCF and  $731.1 \text{ mF cm}^{-2}$  for  $\text{Bi}_2\text{O}_3$ @NPCF. Long-term cycling tests highlighted the superior stability of  $\text{Bi}_2\text{O}_3$ @NPCF, which retained  $\approx 99.6\%$  of its initial capacitance after 10,000 cycles at  $40 \text{ mA cm}^{-2}$ , markedly outperforming NPCF whose retention at  $20 \text{ mA cm}^{-2}$  was only about 56%<sup>[47]</sup> (Figure 4).

In addition, other metal-salt precursors such as  $\text{Fe(OH)}_3$ ,<sup>[70]</sup>  $\text{Mg(OH)}_2$ ,<sup>[71]</sup>  $\text{ZnC}_2\text{O}_4$ ,<sup>[72]</sup>  $\text{Fe(NO}_3)_3$ ,<sup>[73]</sup>  $\text{Mg(Ac)}_2$ ,<sup>[74]</sup> and  $\text{CaCO}_3$ <sup>[75]</sup> can be thermally decomposed into the corresponding metal-oxide templates, producing porous carbons with tunable pore architectures and morphologies. However, the removal of metal-oxide templates typically requires strong-acid etching, a complex and time-consuming process; incomplete removal may result in residual metal contamination that detrimentally affects the purity and electrochemical performance of the porous carbon.

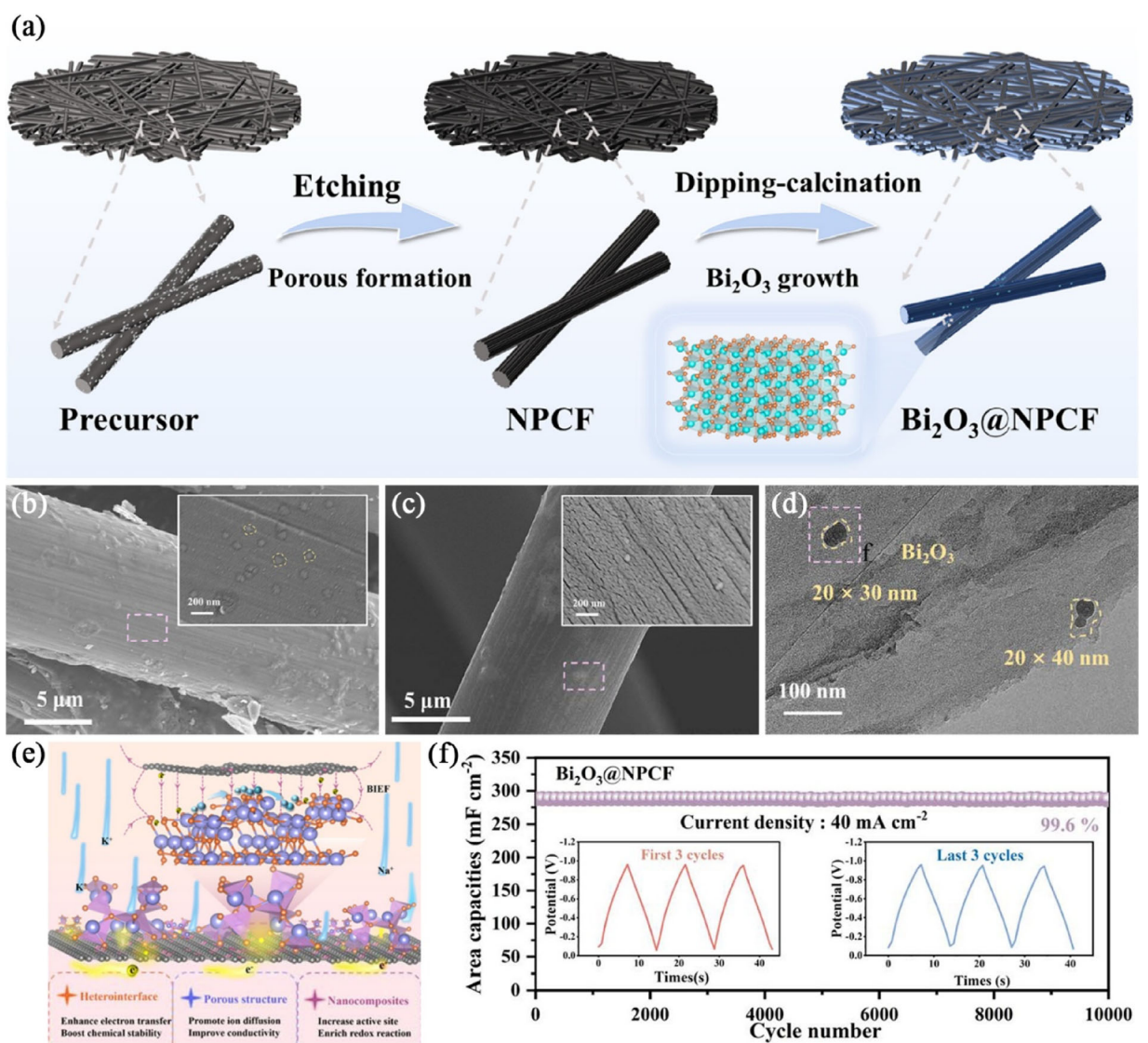


**Figure 4.** a) Schematic of the procedures for the synthesis of NPCF and  $\text{Bi}_2\text{O}_3$ @NPCF. SEM images of b) NPCF and c)  $\text{Bi}_2\text{O}_3$ @NPCF. d) Transmission electron microscope (TEM) images of  $\text{Bi}_2\text{O}_3$ @NPCF. e) Charge storage mechanism of  $\text{Bi}_2\text{O}_3$ @NPCF. f) Long cycling test at  $40 \text{ mA cm}^{-2}$  up to 10,000 cycles for  $\text{Bi}_2\text{O}_3$ @NPCF (Reproduced from ref. [47] with permission from Royal Society of Chemistry).

### 3.1.2. Salt Templates

Salt templates, owing to their good water solubility, can be rapidly removed by mild water washing after carbonization, thereby enabling the porous carbon to precisely retain the pore size and channel distribution imparted by the template. Song et al. used recyclable NaCl as a soluble template and employed polyacrylamide gel as both the carbon and nitrogen source to prepare N/O codoped porous carbon. NaCl was removed by water washing after carbonization, acting as a pore-forming agent that left behind a hierarchical pore structure; meanwhile, N–O functional groups improved the material's wettability and pseudocapacitive contribution. The prepared sample NPC-5 exhibited a BET surface area of  $499.8 \text{ m}^2 \text{ g}^{-1}$  and a specific capacitance of  $283.3 \text{ F g}^{-1}$  at  $0.5 \text{ A g}^{-1}$ . After 10,000 cycles tested at a scan rate of  $200 \text{ mV s}^{-1}$ , NPC-5 retained 93.1% of its capacitance, indicating good electrochemical stability. Moreover, the recyclability of NaCl not only reduced experimental cost but also improved raw-material utilization efficiency.<sup>[52]</sup> Wang et al. employed alkaline lignin as the carbon source, melamine as the nitrogen source, and KCl as the template to produce N-doped lignin-derived porous carbon (LDMCN-700–2). The resulting material exhibited a hierarchical pore architecture, a BET surface area of  $1012.5 \text{ m}^2 \text{ g}^{-1}$  and a high nitrogen content of  $\approx 4.5\%$ . Electrochemical tests showed that LDMCN-700–2 delivered a specific capacitance of  $245 \text{ F g}^{-1}$  at

$0.5 \text{ A g}^{-1}$  and retained 95.7% of its capacity after 5000 cycles at  $20 \text{ mV s}^{-1}$ . This excellent performance is attributed to additional active sites provided by N-doping and to the hierarchical pores that afford good wettability and efficient ion/electron transport.<sup>[76]</sup> Hou et al. used gelatin, a functionalized gel-like biomass precursor, with ZnCl<sub>2</sub> serving both as template and activating agent; after freeze-drying followed by high-temperature carbonization they obtained porous carbon (ZIGC). During freeze-drying, ice-crystal growth helped preserve the 3D pore framework and suppressed ZnCl<sub>2</sub> agglomeration, yielding a high BET surface area ( $1336 \text{ m}^2 \text{ g}^{-1}$ ) while retaining N and O heteroatoms originating from the precursor. Electrochemically, ZIGC exhibited a specific capacitance of  $337.6 \text{ F g}^{-1}$  at  $0.5 \text{ A g}^{-1}$  and maintained 95.6% of its capacitance after 10,000 cycles at  $10 \text{ A g}^{-1}$ <sup>[77]</sup> (Figure 5). Liu et al. used sodium lignosulfonate as the primary carbon source and gelatin as a binder, employing NaNO<sub>3</sub> to act simultaneously as template and activating agent to produce a mesopore-rich, 3D interconnected carbon material. The obtained material displayed a high BET surface area ( $2453.3 \text{ m}^2 \text{ g}^{-1}$ ), a rational pore-size distribution, and efficient ion/electron transport channels, albeit with relatively low heteroatom content, resulting in excellent electrochemical stability. The best sample, LPC-0.5, achieved a specific capacitance of  $166 \text{ F g}^{-1}$  at  $0.5 \text{ A g}^{-1}$  in EMIBF<sub>4</sub> electrolyte and retained 82.5% of its capacitance at an ultrahigh current density of  $50 \text{ A g}^{-1}$ , demonstrating

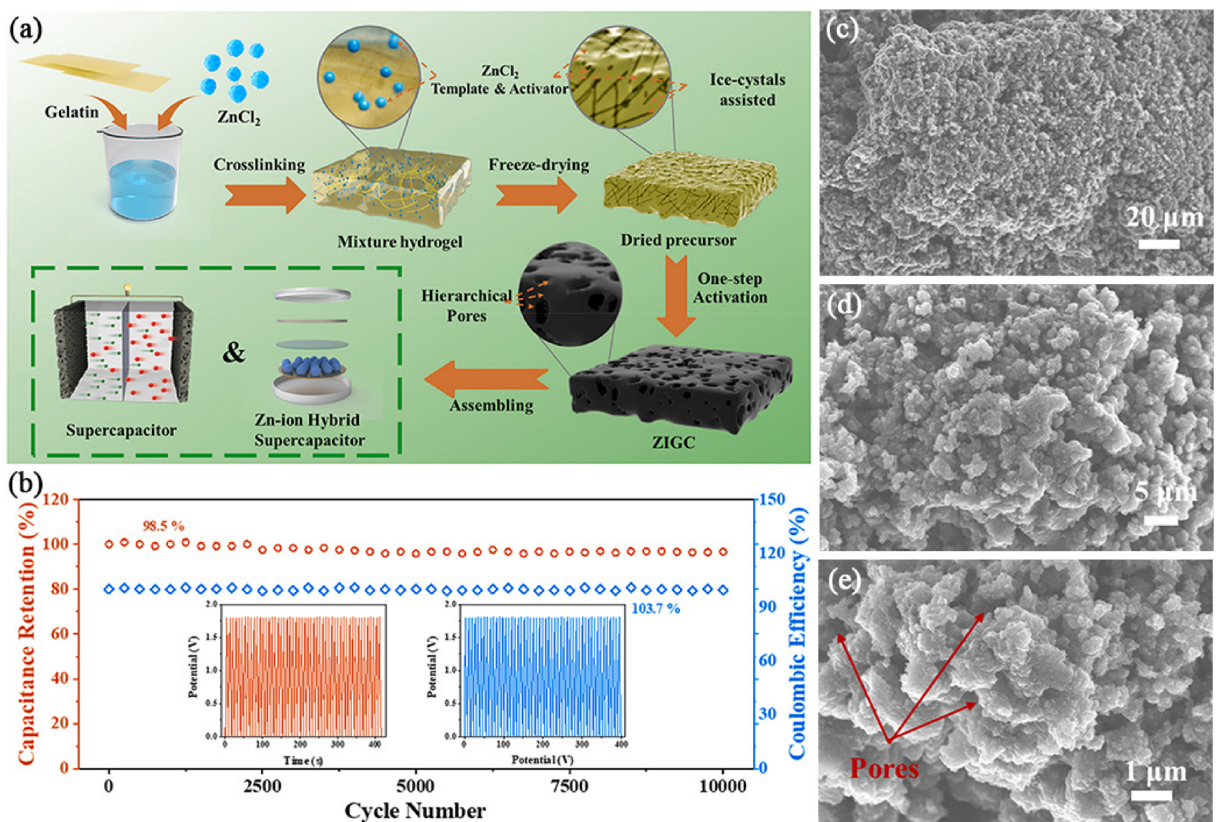


**Figure 5.** a) Schematic illustration of the synthesis procedure of porous carbon with template-activated and ice crystal assisted. b) Cycling test of Zn/ZIGC at  $10 \text{ A g}^{-1}$  (the inset the GCD curves of Zn/ZIGC at the initial 50 cycles of the test and the final 50 cycles). c–e) SEM images of ZIGC (Reproduced from ref. [77] with permission from Elsevier).

good rate capability; as a symmetric device it showed 93.1% capacitance retention after 10,000 cycles at  $2 \text{ A g}^{-1}$ <sup>[78]</sup>.

Salt templates possess intrinsic advantages of low cost, wide availability, and renewability, while their mild and environmentally benign removal process provides a sustainable route for the scalable production of porous carbon.<sup>[79]</sup> However, salts may melt, sinter or undergo grain growth during high-temperature carbonization, which can distort pore morphology and produce nonuniform pore distributions. Therefore, process optimization (e.g., control of temperature, cooling rate and the use of additives) is required to ensure pore-structure uniformity and high material purity.

### 3.1.3. Silica-Based Templates

Among the various hard templates,  $\text{SiO}_2$  is regarded as the most mature template for the synthesis of mesoporous carbon. Li et al. employed inexpensive colloidal  $\text{SiO}_2$  nanoparticles as the template, using glucose as the carbon source and sulfuric acid as a precarbonization reagent and sulfur source, to produce

a low-cost S-doped porous carbon (SPC-900). After carbonization and removal of the  $\text{SiO}_2$  template, SPC-900 exhibited a hierarchical pore architecture and a high BET surface area ( $1125 \text{ m}^2 \text{ g}^{-1}$ ). In a three-electrode configuration, SPC-900 delivered a specific capacitance of  $363 \text{ F g}^{-1}$  at  $0.5 \text{ A g}^{-1}$  and retained 98.1% of its initial specific capacitance after 10,000 cycles at the same current density, demonstrating excellent cycling stability<sup>[57]</sup> (Figure 6). Jin et al. used wheat flour as the precursor and  $\text{SiO}_2$  microspheres of different sizes as templates; following gel-coating and carbonization, they obtained hierarchical porous biomass carbon (HPBC). The close interaction between the spherical  $\text{SiO}_2$  templates and the wheat-flour matrix constrained the formation of the carbon framework during carbonization and imposed spatial orientation, thereby constructing hierarchical pore channels. Benefiting from this structure, the sample HPBC-3 exhibited a BET surface area of  $686 \text{ m}^2 \text{ g}^{-1}$  and showed an optimal specific capacitance of  $223.6 \text{ F g}^{-1}$  at  $1 \text{ A g}^{-1}$ . A symmetric supercapacitor fabricated from HPBC-3 displayed 106% capacitance retention after 5000 cycles in cyclic voltammetry at  $100 \text{ mV s}^{-1}$ <sup>[58]</sup>. Wang et al. prepared lignin-based

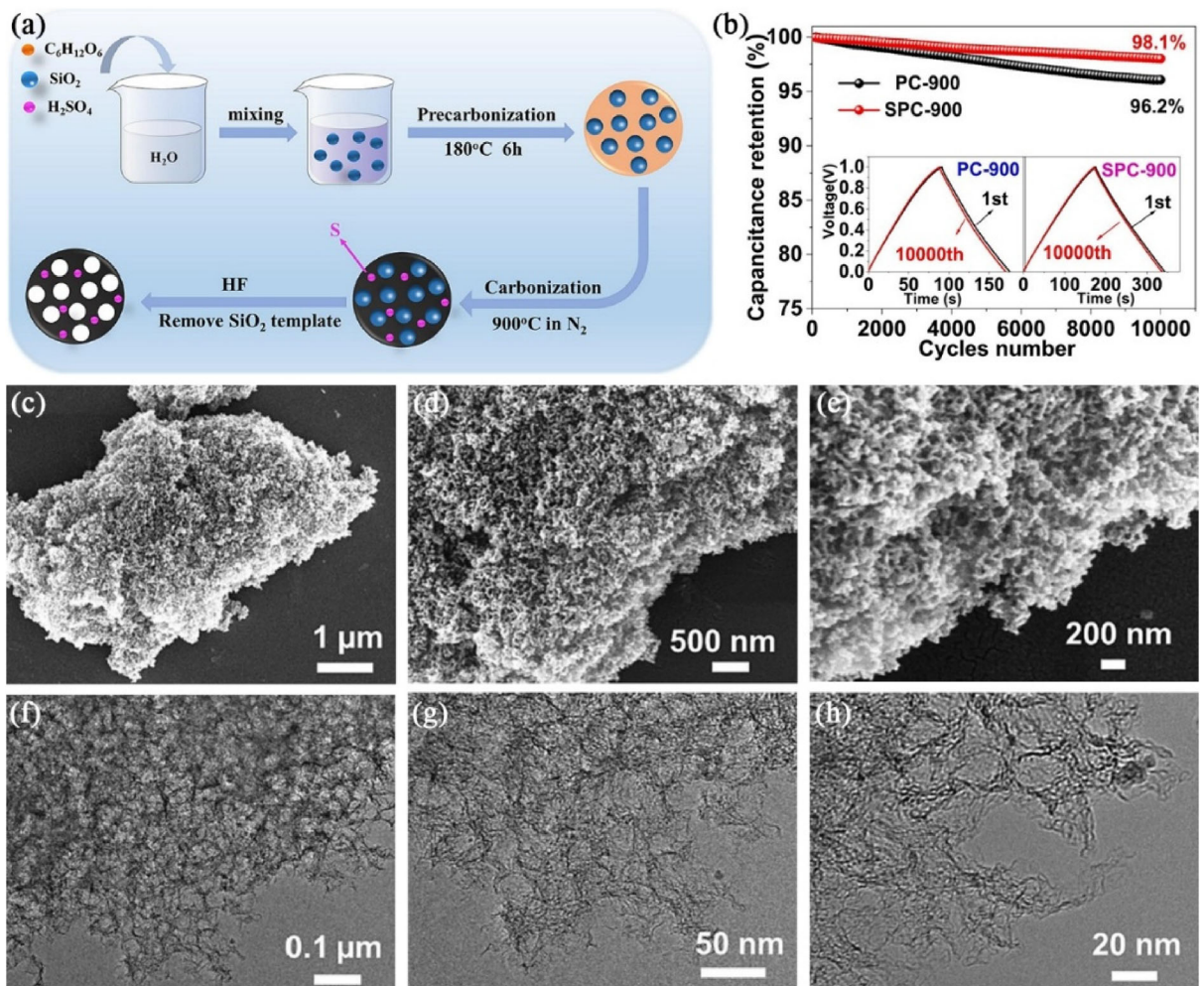


**Figure 6.** a) Schematic illustration of the preparation of S-doped porous carbons. b) Cycling stability of SPC-900 in two-electrode system with  $6.0 \text{ mol L}^{-1}$  KOH. c–e) SEM and f–h) TEM images of SPC-900 (Reproduced from ref. [57] with permission from Elsevier).

fiber aerogels by wet electrospinning and homogeneously embedded  $\text{SiO}_2$  nanospheres within the fibers as templates to construct macropores, while carbonization of lignin generated abundant meso- and microporosity; the result was carbon nanofibers with multiscale porosity. The optimized sample, 100-HPCF, showed marked improvements: a BET surface area of  $779.515 \text{ m}^2 \text{ g}^{-1}$  and a specific capacitance of  $237.1 \text{ F g}^{-1}$  at  $0.5 \text{ A g}^{-1}$ , both substantially superior to the nontemplated lignin-derived electrospun carbon fibers (LESCFs). Moreover, 100-HPCF retained 97.7% of its peak capacitance after 15,000 cycles at  $10 \text{ A g}^{-1}$ <sup>[59]</sup>. Fan et al. applied a one-pot pyrolysis strategy using  $\text{SiO}_2$  nanoparticles as the mesopore template and  $\text{ZnCl}_2$  as the micropore-activating agent to synthesize hierarchical porous carbons (HPCs) with a BET surface area of  $1283 \text{ m}^2 \text{ g}^{-1}$ .  $\text{SiO}_2$  of different particle sizes was used to tune the mesoporous structure, whereas  $\text{ZnCl}_2$  generated abundant micropores within the carbon framework, together producing a hierarchical pore network that effectively enhances charge accumulation in the electrical double layer and thus increases capacitance. The optimized sample, HPC-15, achieved a specific capacitance as high as  $432 \text{ F g}^{-1}$  at  $1 \text{ A g}^{-1}$ ; after 10,000 cycles at  $2 \text{ A g}^{-1}$  it still delivered  $336 \text{ F g}^{-1}$ , corresponding to a capacitance retention of 95.7%.<sup>[60]</sup> However, removal of silicon-based templates commonly relies on hydrofluoric acid etching, which is not only hazardous to operate but also produces fluoride-containing wastewater, posing significant environmental and safety challenges.<sup>[65,80,81]</sup>

### 3.1.4. Polymeric Templates

Polymeric templates impart a controllable porous network to carbon materials through spatial templating. During carbonization, thermal decomposition, and volatilization of the polymer template allow the porous carbon to faithfully preserve pore sizes and morphologies determined by the original template geometry. Wang et al. employed poly(vinyl butyral) (PVB) as both template and crosslinker and lignite as a low-cost precursor to prepare heteroatom-doped HPCs. The optimal sample, HPC-20, featured highly interconnected multiscale channels and a heteroatom-rich surface, with a BET surface area of  $1259 \text{ m}^2 \text{ g}^{-1}$ . Electrochemically, HPC-20 delivered a specific capacitance of  $304 \text{ F g}^{-1}$  at  $0.5 \text{ A g}^{-1}$  and still retained 65.8% of that capacitance even at  $50 \text{ A g}^{-1}$ . Symmetric supercapacitors assembled from HPC-20 exhibited capacitance retentions of 83.5% (in 6 M KOH) and 91.3% (in 1 M  $\text{Na}_2\text{SO}_4$ ) after 10,000 cycles at  $2 \text{ A g}^{-1}$ . The synergy between multiscale porosity and heteroatom doping in HPC-20 enhances electrolyte wetting, ion/electron transport and pseudocapacitive sites, thereby underpinning its fast charge–discharge capability and high energy storage performance.<sup>[63]</sup> Wang et al. also used cellulose nanocrystals (CNC), a phenol–urea–formaldehyde resin (as carbon source) and KOH (as activating agent) to fabricate a hierarchically porous carbon (ARC<sub>CNC</sub>). The CNC template decomposed during carbonization to generate mesopores corresponding to its diameter; together with KOH activation, this produced a synergistic

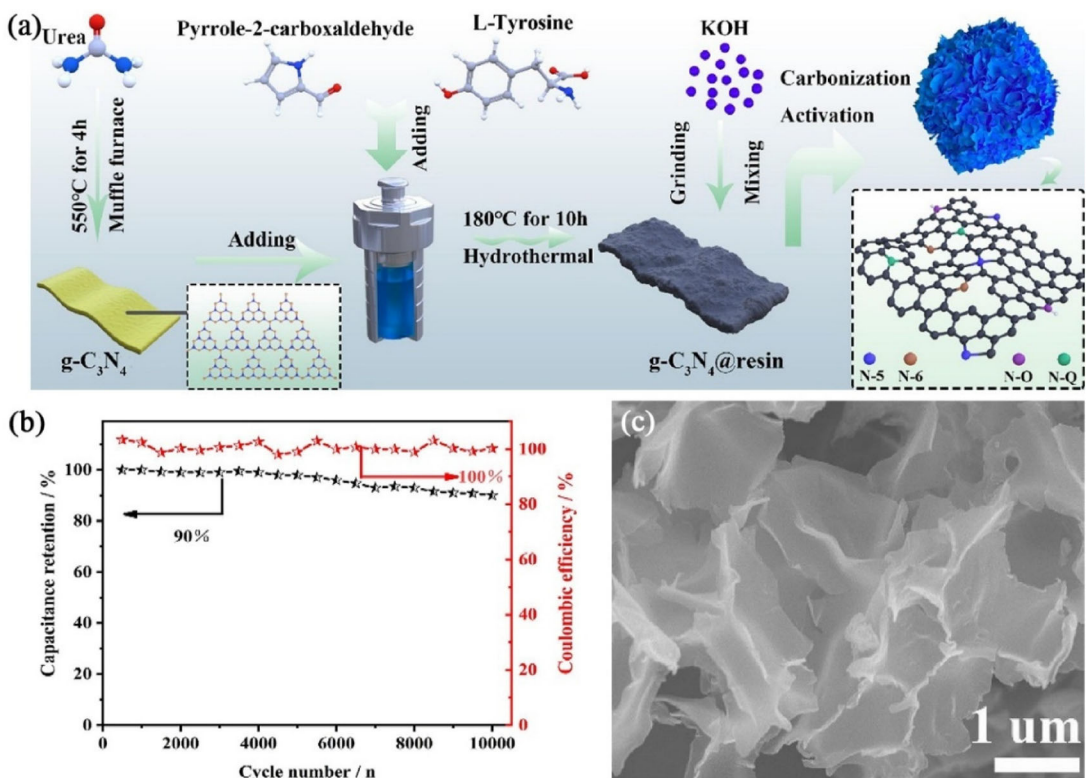


**Figure 7.** a) Schematic diagram of the preparation process of N-PCNs. b) Cycling stability tested at  $10 \text{ A g}^{-1}$  and coulombic efficiency. c) SEM images of N-PCN-800-3 (Reproduced from ref. [83] with permission from Elsevier).

micro/meso/macroporous network. The resulting material exhibited a BET surface area of  $926 \text{ m}^2 \text{ g}^{-1}$ , and when used as a supercapacitor electrode  $\text{ARC}_{\text{CNC}}$  showed a specific capacitance of  $194.9 \text{ F g}^{-1}$  at  $1.0 \text{ A g}^{-1}$ . Even at an ultrahigh current density of  $40.0 \text{ A g}^{-1}$ , the material retained over 74% of its capacitance; moreover, symmetric devices based on  $\text{ARC}_{\text{CNC}}$  maintained  $>95\%$  capacitance retention after 10,000 cycles at  $10.0 \text{ A g}^{-1}$ <sup>[82]</sup>. Li et al. employed  $\text{g-C}_3\text{N}_4$  as a template and an L-tyrosine-based resin as the carbon precursor. After hydrothermal polymerization of the precursor composite followed by KOH chemical activation and carbonization, they obtained nitrogen-rich porous carbon nanosheets ( $\text{N-PCN}_{-800-3}$ ) with a BET surface area as high as  $3542 \text{ m}^2 \text{ g}^{-1}$ . As an electrode, the N-PCNs exhibited a specific capacitance of  $349 \text{ F g}^{-1}$  at  $0.5 \text{ A g}^{-1}$  and still delivered  $218 \text{ F g}^{-1}$  at  $50 \text{ A g}^{-1}$ , demonstrating excellent rate capability. In terms of cycling stability, the specific capacitance remained above 90% after 10,000 consecutive cycles at  $10 \text{ A g}^{-1}$ <sup>[83]</sup> (Figure 7). Despite their ability to construct ordered pore channels, polymeric templates have drawbacks: gaseous byproducts from thermal decomposition can cause uneven etching of pore walls, and residual hydrocarbon fragments may block micropores. Additionally, the synthesis cost of polymer templates can be high, significantly increasing the overall cost of material production.

### 3.1.5. New Emerging Templates

In recent years, novel green hard templates exemplified by ice crystals<sup>[84–86]</sup> and eggshells<sup>[87–89]</sup> have emerged as more environmentally friendly and low-cost options for the fabrication of porous carbon materials, laying the foundation for scalable and sustainable production of porous-carbon electrodes.

Hou et al. proposed an ice-crystal-template-assisted chemical activation strategy in which gelatin, rich in hydrophilic segments and heteroatoms, served as the biomass precursor for preparing hierarchically porous carbon (AGC-2). During freeze-drying, controllable ice crystals generate macropores within the carbon precursor, exposing additional surface area and active sites to the activating agent; subsequent chemical activation and carbonization yield an interconnected micro/meso/macroporous network that preserves N and O heteroatoms from the gelatin and reaches a BET surface area as high as  $2684.5 \text{ m}^2 \text{ g}^{-1}$ . Electrochemically, AGC-2 exhibited a specific capacitance of  $453.7 \text{ F g}^{-1}$  at  $1.0 \text{ A g}^{-1}$ , retained 74.4% of its capacitance in a three-electrode test at  $20.0 \text{ A g}^{-1}$ , and showed 98.8% capacity retention after 10,000 galvanostatic charge-discharge cycles at  $10.0 \text{ A g}^{-1}$ <sup>[86]</sup> (Figure 8). These outstanding performances are primarily ascribed to the synergy among ice-crystal-derived macroporous channels, the large surface area generated by chemical activation, and heteroatom doping, which together improve electrolyte wetting, shorten ion-diffusion paths, and provide pseudocapacitive sites. Zhang et al. used eucalyptus leaves as the carbon source and recovered eggshells from biomass waste as a green biotemplate; by copyrolysis they produced high-performance biomass-derived carbon. Moderate eggshell addition facilitated formation of a hierarchical, honeycomb-like pore morphology, and the optimal sample (ELES0.25) exhibited a large BET surface area of  $971.07 \text{ m}^2 \text{ g}^{-1}$ . In a three-electrode configuration, ELES0.25 delivered  $310 \text{ F g}^{-1}$  at  $0.5 \text{ A g}^{-1}$  and maintained  $232 \text{ F g}^{-1}$  at  $20 \text{ A g}^{-1}$  (capacity retention 74.8%). A symmetric device assembled from ELES0.25 (ELES0.25//ELES0.25) retained 97.38% of its capacitance after 10,000 charge-discharge cycles

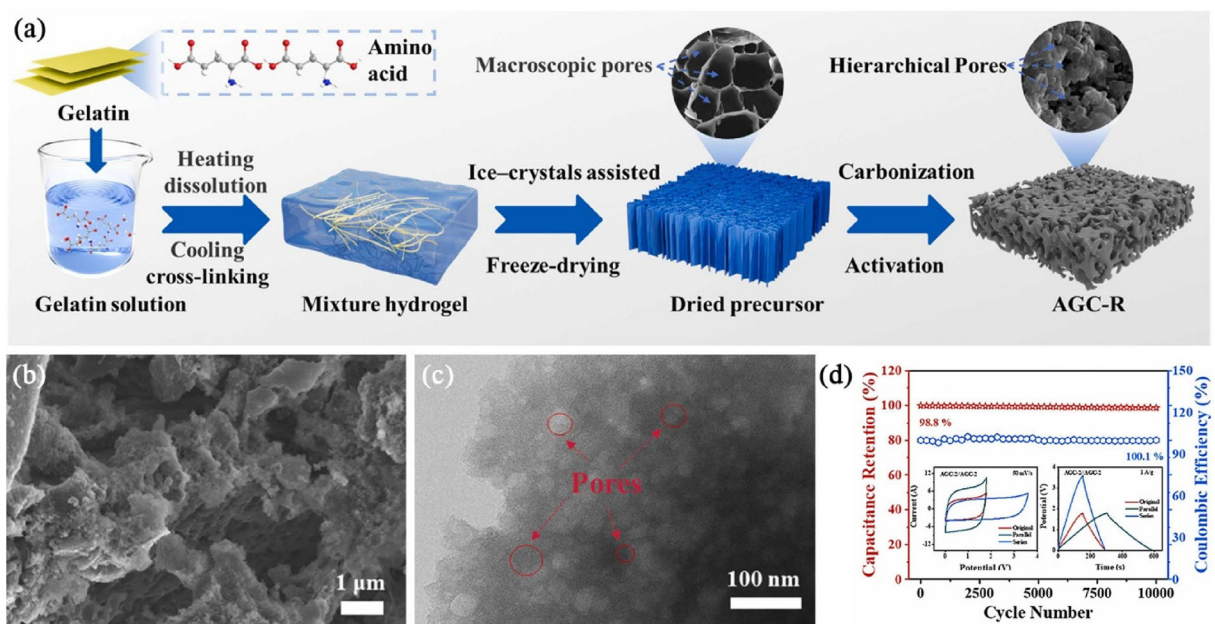


Figure 8. a) Schematic illustration of the synthesis procedure of AGC-R. b) SEM and c) TEM image of AGC-2. d) Cycling test of AGC-2//AGC-2 at  $10 \text{ A g}^{-1}$  (series and parallel experiments of AGC-2//AGC-2 were conducted by connecting of two AGC-2//AGC-2 units) (Reproduced from ref. [86] with permission from Elsevier).

at  $10 \text{ A g}^{-1}$ , demonstrating excellent cycling stability. Overall, using eggshells as a low-cost, eco-friendly template effectively constructs hierarchical channels and markedly enhances the energy-storage performance of biomass-derived carbons.<sup>[89]</sup> Biomass templates combine inherent hierarchical structures, low cost and renewability with intrinsic heteroatoms; when employed as templates and combined with simple chemical treatments, they provide a green and scalable route to porous carbons that simultaneously achieve high surface area, hierarchical porosity, and *in situ* heteroatom doping.

### 3.2. Soft Templates

The soft-template method employs functional organic molecules or supramolecular systems (e.g., surfactants,<sup>[90–92]</sup> block copolymers<sup>[93–96]</sup>) as the central structure-directing agents, which, through hydrogen bonding, hydrophobic/hydrophilic interactions, or electrostatic attractions, guide the cooperative self-assembly of carbon precursors into dynamic ordered structures such as micelles or liquid-crystalline phases. Its core advantages lie in environmentally benign *in situ* pore formation, precise control over mesostructures, and the template is removed during carbonization process.<sup>[97,98]</sup> A typical synthesis procedure involves: 1) dissolving the soft template and carbon precursor in a suitable solvent; 2) inducing cooperative self-assembly under solvent mediation to construct the desired ordered pore channels; and 3) performing high-temperature carbonization under an inert atmosphere, during which the template decomposes and volatilizes, ultimately yielding porous carbons that replicate the structure of the original template.

#### 3.2.1. Surfactant Templates

Surfactant molecules, with their amphiphilic nature, serve as versatile soft templates by dynamically self-assembling into micellar structures that direct the formation of well-defined porous networks in carbon materials. Liang et al. synthesized hollow hierarchical porous carbon spheres (HPCS-900) via a one-pot strategy using alkaline lignin extracted from corn stalks as the carbon precursor, cetyltrimethylammonium bromide (CTAB) as the soft template,  $\text{Zn}^{2+}$  as the crosslinking agent, and potassium bicarbonate ( $\text{KHCO}_3$ ) as the chemical activator. HPCS-900 exhibited a high BET surface area ( $1959 \text{ m}^2 \text{ g}^{-1}$ ) and excellent electrochemical performance, delivering a specific capacitance of  $293 \text{ F g}^{-1}$  at  $0.2 \text{ A g}^{-1}$  with a capacitance retention of 70.8% at  $40 \text{ A g}^{-1}$ . As a supercapacitor electrode, it maintained 86.7% of its capacitance after 10,000 charge-discharge cycles<sup>[91]</sup> (Figure 9). Song et al. developed a soft-template-based directional synthesis strategy to prepare one-dimensional N-doped porous carbon nanorods (N-PCN) with a morphology resembling the single-band structure of "Urechis unicinctus". In this method, the anionic surfactant AOT (sodium bis(2-ethylhexyl) sulfosuccinate) was employed as the template and melamine as the C/N precursor. By precisely tuning the amount of aqueous ammonia ( $\text{NH}_4\text{OH}$ ), the micellar behavior of AOT in water was altered, inducing the formation of rod-like micelles and guiding the directional assembly of 1D carbon frameworks. After thermal treatment and activation, the resulting N-PCN exhibited an ultrahigh BET surface area ( $2560 \text{ m}^2 \text{ g}^{-1}$ ) with a hierarchical porous architecture. Electrochemically, in a three-electrode system N-PCN delivered a specific capacitance of  $398 \text{ F g}^{-1}$  at  $0.5 \text{ A g}^{-1}$  and retained 73.4% of its initial capacitance at  $20 \text{ A g}^{-1}$ . A symmetric supercapacitor assembled from N-PCN

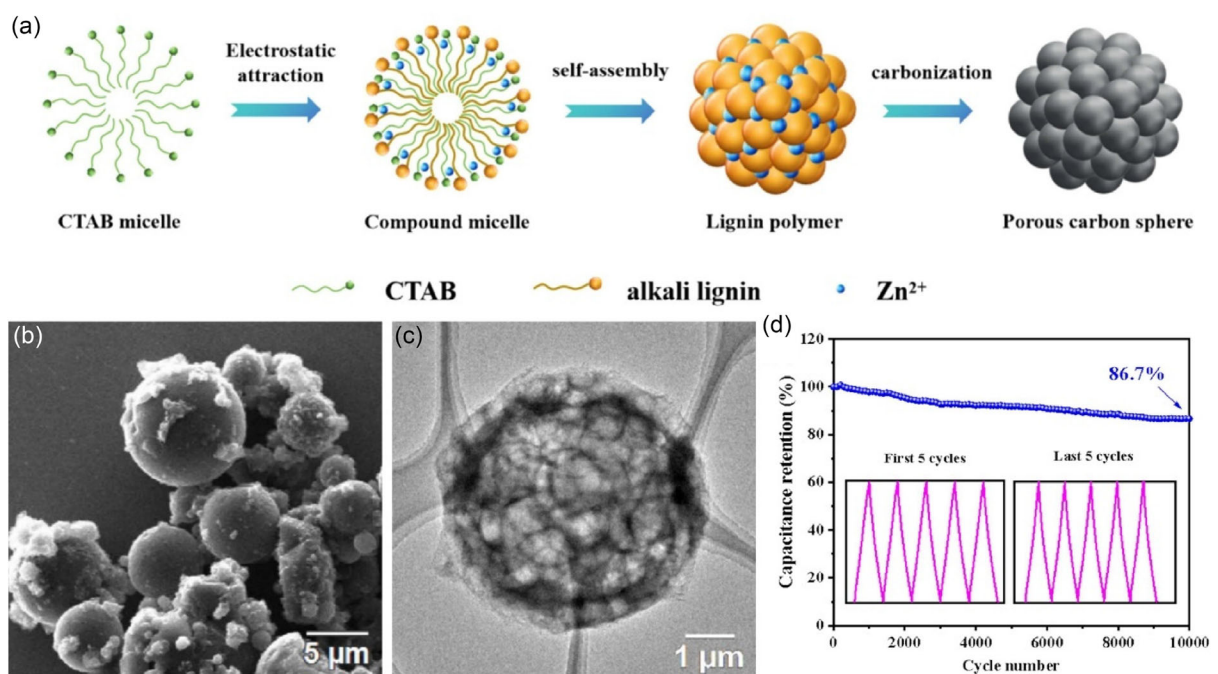


**Figure 9.** a) The schematic illustration of the synthesis process of HPCS. b) SEM c) TEM image of HPCS-900. d) Cycling stability for 5000 cycles of HPCS-900 device (Reproduced from ref. [91] with permission from Elsevier).

in aqueous electrolyte also demonstrated excellent cycling stability, maintaining 94.2% capacitance retention after 10,000 cycles at  $2 \text{ A g}^{-1}$ <sup>[92]</sup>. Li et al. proposed a combined strategy of Triton X-100 soft templating with  $\text{CO}_2$  physical activation to fabricate hierarchical porous carbon nanospheres (AHPCN). In this approach, poly(aniline-co-pyrrole) (PACP) self-assembled at the Triton X-100 micelle interface to form hollow spherical precursors. Subsequent carbonization followed by  $\text{CO}_2$  activation finely tuned micropore formation and overall pore distribution. The optimized sample, AHPCN-3, exhibited a high BET surface area ( $1805 \text{ m}^2 \text{ g}^{-1}$ ) and a specific capacitance of  $135.5 \text{ F g}^{-1}$  at  $0.5 \text{ A g}^{-1}$  in a three-electrode test. Even at a high current density of  $20 \text{ A g}^{-1}$ , it retained  $121.4 \text{ F g}^{-1}$ , demonstrating excellent rate capability. When assembled into symmetric supercapacitors, the system also displayed good cycling durability, with  $\approx 89\%$  capacitance retention after 20,000 cycles.<sup>[90]</sup>

### 3.2.2. Block Copolymer Templates

Block copolymers function as highly designable soft templates by leveraging their intrinsic ability to microphase-separate into diverse, well-ordered nanostructures, which guide the formation

of carbon materials with sophisticated and tunable pore architectures. Zhao et al. proposed a bottlebrush block copolymer (BBCP, PEO-*b*-PDMS)-templating strategy for constructing ordered hierarchical porous structures within carbon nanofiber membranes. By incorporating BBCP into polyacrylonitrile and bridging it with a small-molecule hydrogen-bond donor (HBA), the BBCP self-assembled and dispersed uniformly in the precursor. After electrospinning, preoxidation, carbonization, and BBCP removal, a self-supporting hierarchical porous carbon nanofiber membrane (PCNFs) was obtained. This membrane possessed a BET surface area of  $441.8 \text{ m}^2 \text{ g}^{-1}$ , hierarchical porosity, and high levels of nitrogen and oxygen doping, making it suitable for binder-free electrode applications. Electrochemical tests revealed that PCNFs-1.5 delivered a specific capacitance of  $234.1 \text{ F g}^{-1}$  at  $1 \text{ A g}^{-1}$ , with a capacitance retention of 67.72% at  $50 \text{ A g}^{-1}$  relative to  $1 \text{ A g}^{-1}$ . When applied in aqueous symmetric supercapacitors, PCNFs-1.5 exhibited exceptional durability, retaining over 95% of its capacitance after 55,000 charge-discharge cycles at  $5 \text{ A g}^{-1}$ <sup>[95]</sup> (Figure 10). Wang et al. employed fulvic acid (FA) as the carbon source and P123 as the soft template, combined with KOH activation, to fabricate 3D hierarchical porous carbons (FPs). The optimized sample, FP800, exhibited an ultrahigh BET surface

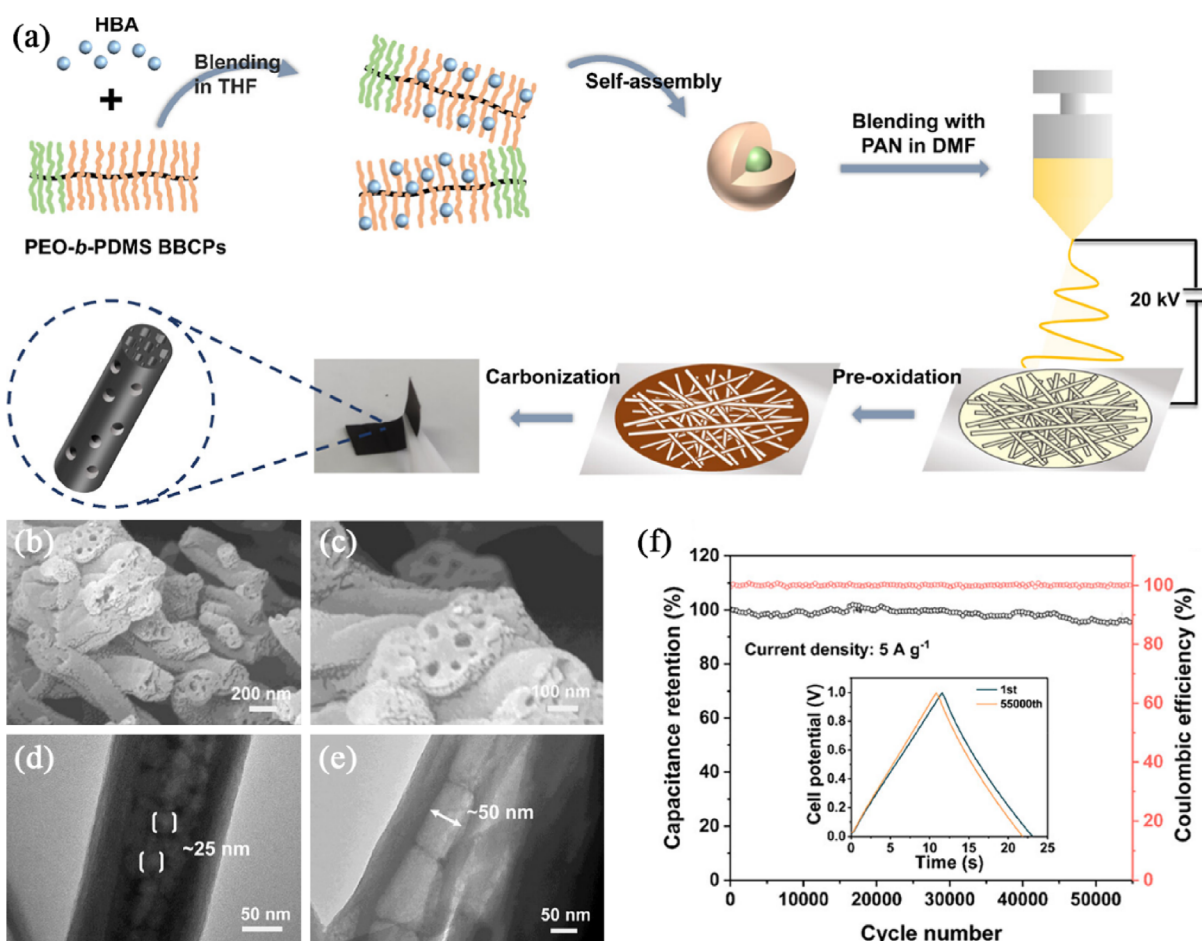


Figure 10. a) Fabrication of the flexible PCNFs. b,c) SEM and d,e) TEM images of PCNFs-1.5. f) Cycling stability of PCNFs-1.5//PCNFs-1.5 at a current density of  $5 \text{ A g}^{-1}$ . Inset: GCD curves of the first and 55,000th cycle (Reproduced from ref. [95] with permission from American Chemical Society).

area of  $1938 \text{ m}^2 \text{ g}^{-1}$  and excellent electrochemical performance, delivering a specific capacitance of  $107 \text{ F g}^{-1}$  at  $1 \text{ A g}^{-1}$  and retaining 90.6% capacitance after 60,000 cycles.<sup>[93]</sup> Wu et al. developed an approach combining the F127 soft template with chemical foaming (assisted by  $\text{NH}_4\text{Cl}$ ) to synthesize ordered mesoporous nitrogen-doped porous carbons (N-HPC) from liquefied wood-derived oligomeric polyols. In this strategy,  $\text{NH}_4\text{Cl}$  enhanced the interaction between the carbon source and the soft template during hydrothermal treatment and pretreatment, thereby promoting the formation of ordered mesopores. During carbonization,  $\text{NH}_4\text{Cl}$  decomposed into  $\text{NH}_3$  and  $\text{HCl:NH}_3$  facilitated N-doping, while the released gases helped generate micropores. The resulting N-HPC-2 exhibited a high BET surface area of  $1160 \text{ m}^2 \text{ g}^{-1}$ . Electrochemical evaluation showed that N-HPC-2 achieved a specific capacitance of  $282 \text{ F g}^{-1}$  at  $1 \text{ A g}^{-1}$  and demonstrated excellent rate performance. Even at a high current density of  $10 \text{ A g}^{-1}$ , its specific capacitance remained nearly unchanged after 5000 cycles.<sup>[94]</sup>

### 3.2.3. Emulsion Templates

Emulsion systems, particularly high internal phase emulsions (HIPEs), act as macroscopic soft templates by establishing a co-continuous interface between immiscible liquids, which is replicated into carbon frameworks to create pervasive, interconnected porosity. Zhao et al. employed a HIPE templating strategy to synthesize N-doped hierarchical porous carbons (NHPCs) using sucrose or glucose together with methacrylic resin,

denoted as S-NHPCs and G-NHPCs, respectively. In this method, sucrose/glucose, formaldehyde, and methacrylic acid formed the continuous HIPE phase in water, which underwent acid-catalyzed condensation and crosslinking to yield porous resins. Subsequent carbonization and activation produced NHPCs with hierarchical porosity. The introduction of biomass carbohydrates not only contributed to the framework formation but also enhanced surface area and hydrophilicity, thereby improving electrochemical properties. Optimized samples exhibited high BET surface areas (S-NHPC-2:  $1682 \text{ m}^2 \text{ g}^{-1}$ ; G-NHPC-3:  $1913 \text{ m}^2 \text{ g}^{-1}$ ) and specific capacitances of 305 and  $262 \text{ F g}^{-1}$  at  $1 \text{ A g}^{-1}$ , respectively. Notably, S-NHPC-2 retained 92.5% of its capacitance after 5000 cycles<sup>[99]</sup> (Figure 11). Zhao et al. further proposed a facile HIPE-template route to prepare N/S co-doped porous carbons (NSPC-2) derived from resorcinol–methylurea–formaldehyde–thiourea (RMFT) resins. When the molar ratio of thiourea to methylurea (T/M) was optimized at 2:1, the resulting sample achieved a BET surface area of  $1721 \text{ m}^2 \text{ g}^{-1}$ , delivering a specific capacitance of  $213.5 \text{ F g}^{-1}$  at  $1 \text{ A g}^{-1}$  and maintaining  $166.2 \text{ F g}^{-1}$  at  $10 \text{ A g}^{-1}$ , demonstrating excellent rate capability. More importantly, this NSPC retained 99.6% of its capacitance after 10,000 charge-discharge cycles at  $10 \text{ A g}^{-1}$ , highlighting outstanding cycling stability.<sup>[100]</sup> Addressing the limitation of conventional HIPE-derived carbons, which often exhibit excessive macroporosity and relatively low surface area, Zhao et al. proposed an improved interphase–external phase coupled HIPE (IP-EP coHIPE) strategy to enhance textural properties. In this method, sodium alginate (SA) aqueous solution was used as the internal phase, while a divinylbenzene (DVB)-containing oil phase served as the external

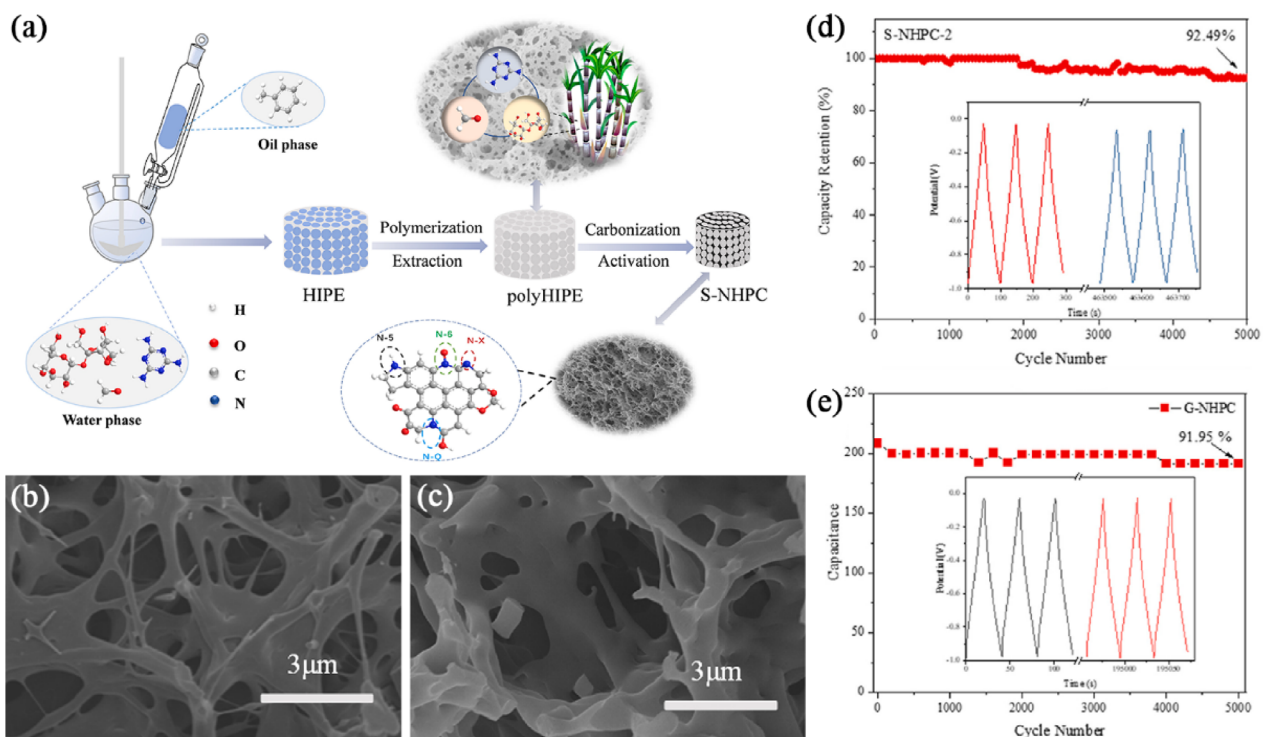


**Figure 11.** a) Schematic illustration of the preparation of S/G-NHPCs using HIPE template. SEM images of b) S-NHPC-2 and c) G-NHPC-3 derived from polyHIPEs. Cycle performance of d) S-NHPC-2 and e) G-NHPC-3 (Reproduced from ref. [99] with permission from Elsevier).

phase. Sequential external-phase polymerization, internal-phase crosslinking, and carbonization produced polymer-derived HPCs. Upon optimization, the representative sample HPC-85/1.5 exhibited an ultrahigh BET surface area of  $2289 \text{ m}^2 \text{ g}^{-1}$  and a specific capacitance of  $306 \text{ F g}^{-1}$  at  $1 \text{ A g}^{-1}$ . Even after 10,000 cycles at  $10 \text{ A g}^{-1}$ , it retained 99.6% of its capacitance. These results underscore the effectiveness and potential of the IP-EP coHIPE strategy for producing high-performance HPC electrodes.<sup>[101]</sup>

### 3.3. Self-Templates

The self-templating method is an innovative strategy that exploits the intrinsic structure of materials as built-in templates to synthesize porous carbons. Unlike conventional hard- or soft-template approaches that rely on external templating agents, this method employs rational chemical design to transform specific components within the precursor into pore-forming units, thereby enabling the construction of porous architectures without the need for exogenous templates.<sup>[43]</sup> This process eliminates the complex post-treatment typically required in traditional templating methods, markedly simplifying the synthesis procedure and reducing environmental impact.

#### 3.3.1. MOF-Derived Carbons

MOFs have attracted significant attention as self-templates for the preparation of carbon materials in energy storage

applications.<sup>[102]</sup> MOFs possess designable metal nodes and organic ligands, ordered pore structures, and high surface areas; by selecting appropriate metal-ligand combinations and tailoring the thermal treatment pathway, the composition, pore architecture, and heteroatom doping of the resulting carbons can be precisely controlled. During pyrolysis, the organic ligands carbonize to form the carbon framework, while the *in situ* migration or removal of the metal species not only generates hierarchical porosity but also catalyzes local graphitization, thereby shortening electron/ion transport pathways and enhancing rate performance. Ghosh et al. used Zn-BTC-BPY as both self-sacrificing template and precursor, and carbonized it sequentially at 700, 850, and 1000 °C to obtain a series of defect-rich N-doped porous carbons (N-PCs). Subsequent acid washing removed inorganic residues to improve electrolyte accessibility. With increasing carbonization temperature, defect density increased while nitrogen content decreased. The optimal sample, N-PC-1000, exhibited a BET surface area of  $\approx 408 \text{ m}^2 \text{ g}^{-1}$  and delivered a specific capacitance of  $151 \text{ F g}^{-1}$  at  $1 \text{ A g}^{-1}$  in a three-electrode system. Furthermore, it retained over 98% of its capacity after 10,000 galvanostatic charge-discharge cycles<sup>[103]</sup> (Figure 12). Gang et al. directly carbonized the Zn-TDPAT [Zn-2,4,6-tris(3,5-dicarboxyphenylamino)-1,3,5-triazine] MOF to prepare nitrogen-rich spherical porous carbons (NSPCs) without employing additional dopants, templates, acid/base washing, or activation treatments. During carbonization, the removal of metal species and partial functional groups generated an *in situ* micro/mesoporous

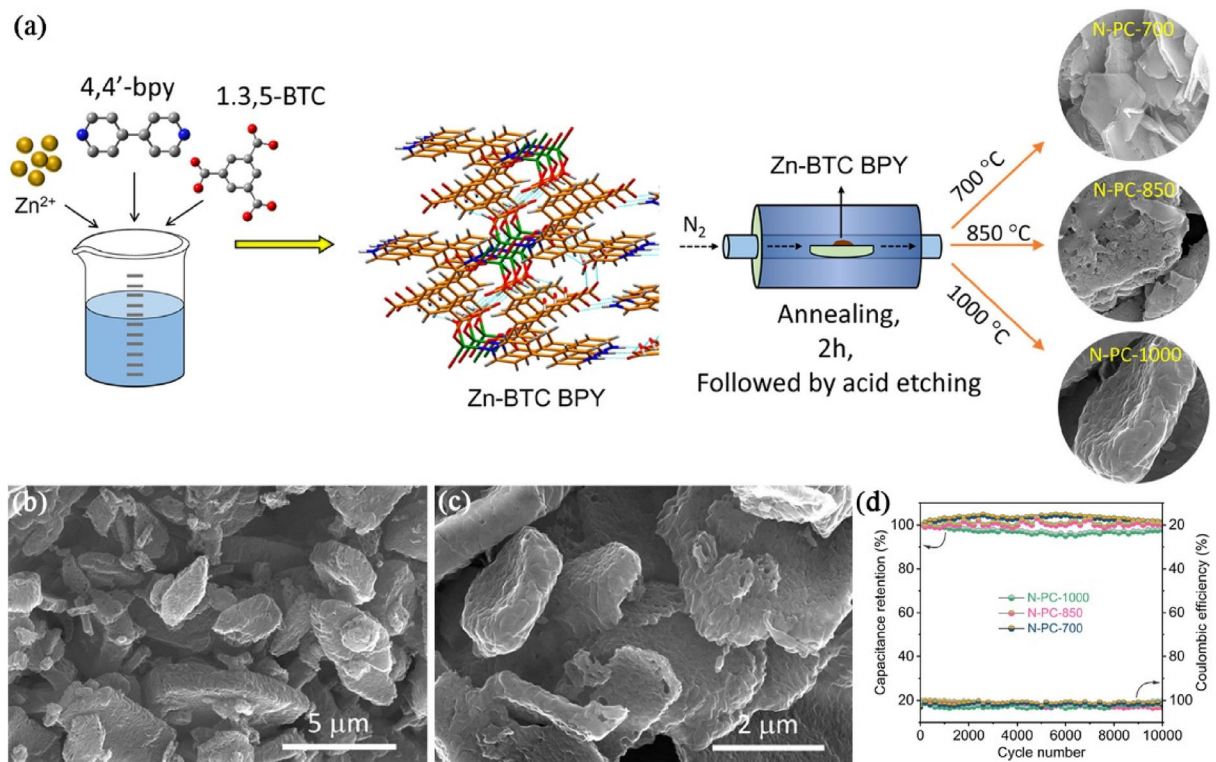


**Figure 12.** a) Schematic illustration of the synthesis of Zn-BTC BPY derived nitrogen doped porous carbons (N-PC-700, N-PC-850 and N-PC-1000). b,c) FESEM images of N-PC-1000. d) Cyclic stability and coulombic efficiency of N-PC-700, N-PC-850 and N-PC-1000 electrodes calculated for 10,000 GCD cycles at a current density of  $8 \text{ A g}^{-1}$  using 2 M KOH electrolyte (Reproduced from ref. [103] with permission from Elsevier).

network, yielding a hierarchical structure with excellent electrolyte accessibility. The resulting NSPC exhibited a high BET surface area of  $1826 \text{ m}^2 \text{ g}^{-1}$  and a specific capacitance of  $386.3 \text{ F g}^{-1}$  at  $1 \text{ A g}^{-1}$  in a three-electrode test. More importantly, even under harsh long-term cycling conditions ( $150 \text{ A g}^{-1}$ , 100,000 cycles), it maintained 97.8% of its capacitance, demonstrating outstanding cycling stability.<sup>[104]</sup> Kolachi et al. proposed a strategy to achieve superior electrochemical performance by precisely tuning Mg/Zn bimetallic MOF-derived structures. The approach combines adjustment of the Mg/Zn ratio, decarboxylation and removal of volatile species, dezincification and KOH activation to synergistically control the formation and transformation of micropores and mesopores. The optimized sample MZAPC-4 exhibited an ultrahigh BET surface area of  $2127.6 \text{ m}^2 \text{ g}^{-1}$  and delivered a high specific capacitance of  $468 \text{ F g}^{-1}$  at  $1 \text{ A g}^{-1}$  in three-electrode testing. Furthermore, the material retained excellent rate capability at ultrahigh current densities and preserved  $\approx 84.3\%$  of its initial capacitance after 100,000 cycles at  $100 \text{ A g}^{-1}$ , demonstrating outstanding long-term cycling stability.<sup>[105]</sup> Jiang et al. proposed a green preionization synthesis strategy to prepare a Mg and Al bimetallic MOF and, through controlled carbonization and demetalation, obtained layered hierarchical porous carbon (RPC). The method avoids high temperature, high pressure and organic solvents, thereby facilitating scale-up and low-energy production. By tuning the Mg/Al ratio and the pyrolysis conditions, the authors achieved fine control over particle size, pore-size distribution and interlayer spacing of the carbon layers, which in turn optimized charge storage and ion transport channels. The optimized material RPC-2 exhibited a high BET surface area of  $1035 \text{ m}^2 \text{ g}^{-1}$  and delivered an excellent specific capacitance of  $434 \text{ F g}^{-1}$  at

$1 \text{ A g}^{-1}$  when employed as a supercapacitor electrode. In long-term cycling tests RPC-2 showed outstanding stability, retaining  $\approx 96\%$  of its capacitance after 100,000 cycles at  $100 \text{ A g}^{-1}$ .<sup>[106]</sup>

### 3.3.2. Biomass-Derived Carbons

Biomass has also received extensive attention as a self-template for the preparation of carbon materials in energy storage. Compared with purely synthetic precursors, biomass inherently contains abundant and naturally hierarchical microstructures as well as heteroatom sites. During high-temperature pyrolysis and activation, the cell walls, fibers, or cavity structures of biomass are preserved or enlarged through the expulsion of volatile components and the reconstruction of the carbon framework, enabling natural macro-/microporous channels to directly act as templates for hierarchical porosity. Meanwhile, intrinsic heteroatoms such as N, O, and S within biomass can be directly incorporated into the carbon framework during carbonization or activation, thereby improving surface chemistry, enhancing wettability, and introducing pseudocapacitive sites, which together boost conductivity and electrochemical performance. Combined with advantages of wide availability, low cost, and renewability, biomass self-templating offers an economical and environmentally friendly pathway to produce HPCs with high surface area, excellent ion accessibility, and scalability potential for electrode applications.<sup>[107]</sup> Zhao et al. proposed a multiscale self-templating route using potassium-modified sodium lignosulfonate (KLS), derived from waste lignosulfonate, as the precursor. By introducing carboxyl groups and generating in situ template

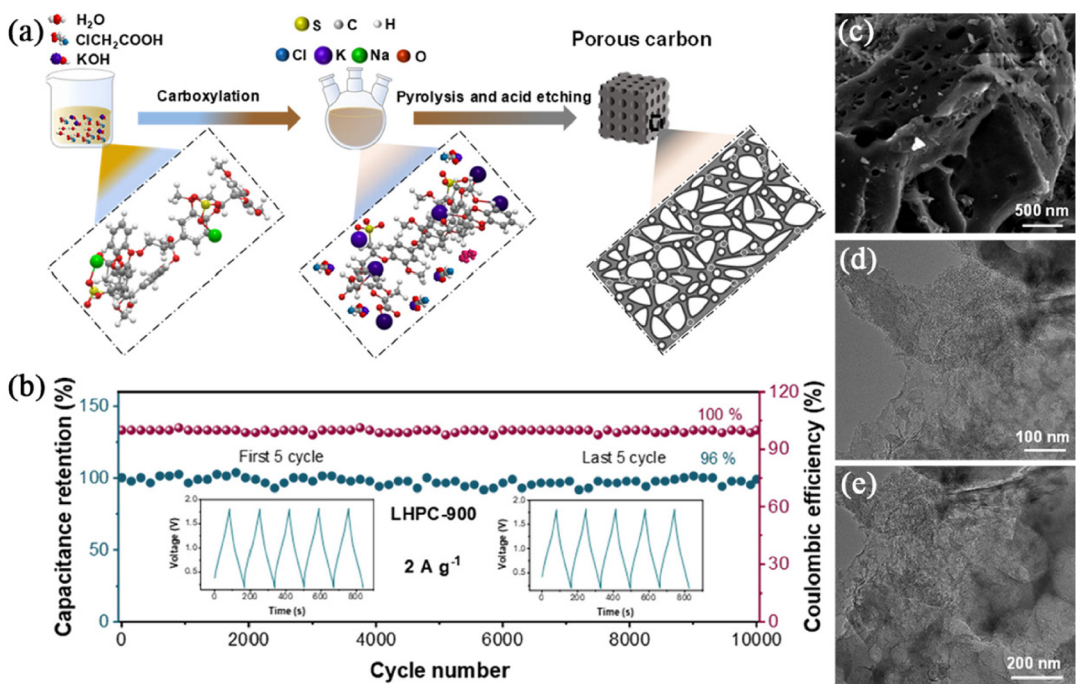


**Figure 13.** a) Schematic illustration for preparation of LHPC-700, LHPC-800, and LHPC-900. b) Long-term cycle performance of LHPC-900 at a current density of  $2 \text{ A g}^{-1}$  (The insets show the first five and the last five charge/discharge cycles). c) SEM and d,e) TEM images of LHPC-900 (Reproduced from ref. [108] with permission from Elsevier).

salts ( $\text{KCl}$ ,  $\text{K}_2\text{CO}_3$ , and sulfates) during pyrolysis, hierarchical pore architectures were constructed from the molecular to the macroscopic scale. This strategy utilized a papermaking byproduct as a sustainable carbon source, while the sacrificial template salts induced the formation of abundant micro/meso/macroporous networks. The optimized sample, LHPG-900, exhibited an ultrahigh surface area of  $2460 \text{ m}^2 \text{ g}^{-1}$  and, when applied as a supercapacitor electrode, delivered a capacitance of  $\approx 298 \text{ F g}^{-1}$  at  $0.1 \text{ A g}^{-1}$ , retaining  $\approx 97\%$  of its capacity after 8000 cycles at  $2 \text{ A g}^{-1}$ <sup>[108]</sup> (Figure 13). Yue et al. employed bamboo and shrimp shells as raw materials, with  $\text{KHCO}_3$  as a green activating agent, to prepare N/O codoped porous carbons (KBP). In this system,

shrimp shells served as a self-template: proteins and chitin provided heteroatom sources, while  $\text{CaCO}_3$  acted as a sacrificial hard template to mediate pore formation. The optimal sample, BC-SP-1, exhibited a high surface area of  $1194.2 \text{ m}^2 \text{ g}^{-1}$  and a specific capacitance of  $311.45 \text{ F g}^{-1}$  at  $0.5 \text{ A g}^{-1}$ . In a three-electrode system, the electrode retained 87.5% of its capacity after 5000 charge-discharge cycles at  $10 \text{ A g}^{-1}$ <sup>[109]</sup>. Jiao et al. proposed a combined multistep carbonization and mild activation route, using the naturally layered structure of nitrogen-rich soybean straw as a self-template to prepare HPC. By tuning carbonization and activation conditions, the resulting sample SSC-700 achieved a surface area of  $2012.6 \text{ m}^2 \text{ g}^{-1}$  and delivered a capacitance of

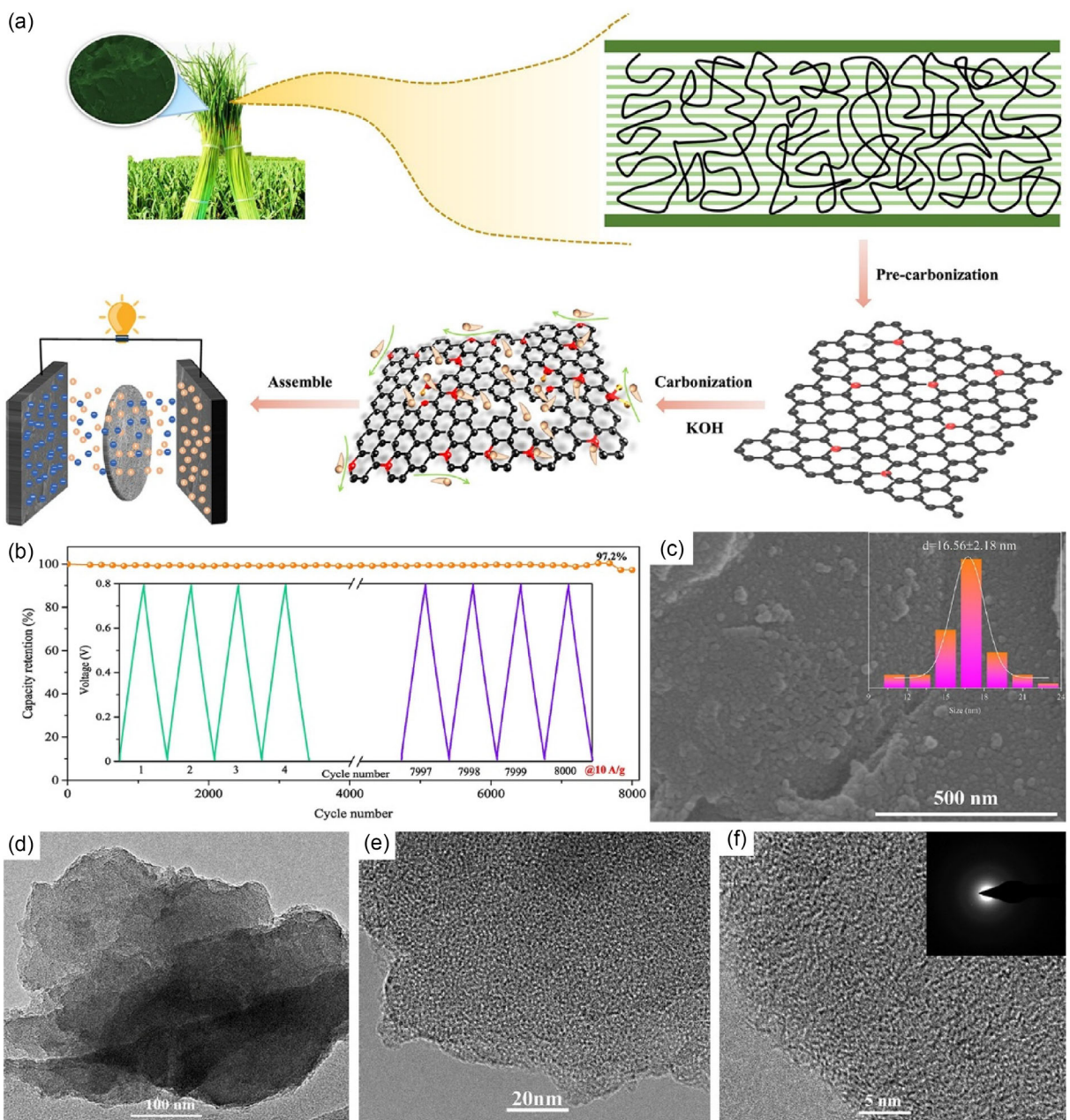


**Figure 14.** a) Schematic illustration of GPCs preparation by one-step carbonization and activation. b) Cycling stability of GPC-4. c) SEM, d) TEM, and e,f) High-resolution TEM images of GPC-4 (Reproduced from ref. [113] with permission from Elsevier).

380.5 F g<sup>-1</sup> at 0.5 A g<sup>-1</sup> in a three-electrode system. Furthermore, SSC-700 retained 73.97% of its capacitance after 10,000 cycles at 10 A g<sup>-1</sup>[110]. Sun et al. developed a strategy using mantis shrimp shell ash as a self-template, combined with the directional assembly of chitosan-derived carbon aerogels. Guided by the ordered pore channels of the shrimp-shell ash, chitosan self-assembled into a pore-array precursor; subsequent removal of CaCO<sub>3</sub> from the shells and KOH activation yielded hierarchically porous

carbons rich in N and O heteroatoms. The representative sample, BAPC-800, exhibited an ultrahigh surface area of 2951 m<sup>2</sup> g<sup>-1</sup> and delivered a specific capacitance of 401 F g<sup>-1</sup> at 0.5 A g<sup>-1</sup> in a three-electrode system. Remarkably, it retained 97.3% of its capacitance after 10,000 cycles at 5 A g<sup>-1</sup>, demonstrating outstanding long-term stability.[111] Xu et al. proposed a facile two-step self-templated carbonization strategy that exploits the intrinsic vascular-bundle architecture of bagasse as an

**Table 1.** Capacitance performances of obtained porous carbon using three types of template strategies.

Material	Template	SSA [m <sup>2</sup> g <sup>-1</sup> ]	Specific capacitance	Cyclic stability	Reference
NPPC-700	MnO <sub>2</sub>	142.97	398.11 F cm <sup>-3</sup> at 0.5 A g <sup>-1</sup>	93.12% after 10,000 cycles at 5 A g <sup>-1</sup>	[66]
CHPC-2	MgO	1190	199.0 F g <sup>-1</sup> at 1 A g <sup>-1</sup>	98.5% after 20,000 cycles at 6 A g <sup>-1</sup>	[51]
NP-HPC-2	ZnO	999.66	394.51 F g <sup>-1</sup> at 0.2 A g <sup>-1</sup>	95.7% after 10,000 cycles at 5 A g <sup>-1</sup>	[67]
BTC-0.2-2-800	Al <sub>2</sub> O <sub>3</sub>	1713.1	292.1 F g <sup>-1</sup> at 1 A g <sup>-1</sup>	no significant capacity degradation after 10,000 cycles at 10 A g <sup>-1</sup>	[68]
NNHPC-1CaO	CaO	3117.73	429.18 F g <sup>-1</sup> at 0.2 A g <sup>-1</sup>	99.51% after 10,000 cycles at 10 A g <sup>-1</sup>	[69]
NPC-5	NaCl	499.8	283.3 F g <sup>-1</sup> at 0.5 A g <sup>-1</sup>	93.1% after 10,000 cycles at 200 mV s <sup>-1</sup>	[52]
LDMCN-700-2	KCl	1012.5	245 F g <sup>-1</sup> at 0.5 A g <sup>-1</sup>	95.7% after 5000 cycles at 20 mV s <sup>-1</sup>	[76]
ZIGC	ZnCl <sub>2</sub>	1336	337.6 F g <sup>-1</sup> at 0.5 A g <sup>-1</sup>	95.6% after 10,000 cycles at 10 A g <sup>-1</sup>	[77]
LPC-0.5	NaNO <sub>3</sub>	2453.3	166 F g <sup>-1</sup> at 0.5 A g <sup>-1</sup>	93.1% after 10,000 cycles at 2 A g <sup>-1</sup>	[78]
SPC-900	SiO <sub>2</sub>	1125	363 F g <sup>-1</sup> at 0.5 A g <sup>-1</sup>	98.1% after 10,000 cycles at 0.5 A g <sup>-1</sup>	[57]
HPBC-3	SiO <sub>2</sub>	686	223.6 F g <sup>-1</sup> at 1 A g <sup>-1</sup>	106% after 5000 cycles at 100 mV s <sup>-1</sup>	[58]
100-HPCF	SiO <sub>2</sub>	779.515	237.1 F g <sup>-1</sup> at 0.5 A g <sup>-1</sup>	97.7% after 15,000 cycles at 10 A g <sup>-1</sup>	[59]
HPC-15	SiO <sub>2</sub>	1283	432 F g <sup>-1</sup> at 1 A g <sup>-1</sup>	95.7% after 10,000 cycles at 2 A g <sup>-1</sup>	[60]
HPC-20	PVB	1259	304 F g <sup>-1</sup> at 0.5 A g <sup>-1</sup>	91.3% after 10,000 cycles at 2 A g <sup>-1</sup>	[63]
ARC <sub>CNC</sub>	CNC	926	194.9 F g <sup>-1</sup> at 1 A g <sup>-1</sup>	over 95% after 10,000 cycles at 10 A g <sup>-1</sup>	[82]
N-PCN-800-3	g-C <sub>3</sub> N <sub>4</sub>	3542	349 F g <sup>-1</sup> at 0.5 A g <sup>-1</sup>	90% after 10,000 cycles at 10 A g <sup>-1</sup>	[83]
AGC-2	ice	2684.5	453.7 F g <sup>-1</sup> at 1 A g <sup>-1</sup>	98.8% after 10,000 cycles at 10 A g <sup>-1</sup>	[86]
ELES0.25	eggshell	971.07	310 F g <sup>-1</sup> at 0.5 A g <sup>-1</sup>	97.38% after 10,000 cycles at 10 A g <sup>-1</sup>	[89]
HPCS-900	CTAB	1959	293 F g <sup>-1</sup> at 0.2 A g <sup>-1</sup>	86.7% after 10,000 cycles	[91]
N-PCN	AOT	2560	398 F g <sup>-1</sup> at 0.5 A g <sup>-1</sup>	94.2% after 10,000 cycles at 2 A g <sup>-1</sup>	[92]
AHPCN-3	Triton X-100	1805	135.5 F g <sup>-1</sup> at 0.5 A g <sup>-1</sup>	89% after 20,000 cycles	[90]
PCNFs-1.5	BBCP	441.8	234.1 F g <sup>-1</sup> at 1 A g <sup>-1</sup>	over 95% after 55,000 cycles at 5 A g <sup>-1</sup>	[95]
FP800	P123	1938	107 F g <sup>-1</sup> at 1 A g <sup>-1</sup>	90.6% after 60,000 cycles at 2.5 A g <sup>-1</sup>	[93]
N-HPC-2	F127	1160	282 F g <sup>-1</sup> at 1 A g <sup>-1</sup>	almost the same after 5000 cycles at 10 A g <sup>-1</sup>	[94]
S-NHPC-2	HIPE	1682	305 F g <sup>-1</sup> at 1 A g <sup>-1</sup>	92.5% after 5000 cycles at 5 A g <sup>-1</sup>	[99]
NSPC-2	HIPE	1721	213.5 F g <sup>-1</sup> at 1 A g <sup>-1</sup>	99.6% after 10,000 cycles at 10 A g <sup>-1</sup>	[100]
HPC-85/1.5	HIPE	2289	306 F g <sup>-1</sup> at 1 A g <sup>-1</sup>	99.6% after 10,000 cycles at 10 A g <sup>-1</sup>	[101]
N-PC-1000	Zn-BTC-BPY	408	151 F g <sup>-1</sup> at 1 A g <sup>-1</sup>	98% after 10,000 cycles at 8 A g <sup>-1</sup>	[103]
NSPC	Zn-TDPAT	1826	386.3 F g <sup>-1</sup> at 1 A g <sup>-1</sup>	97.8% after 100,000 cycles at 150 A g <sup>-1</sup>	[104]
MZAPC-4	Mg <sub>2</sub> Zn <sub>3</sub> -MOF	2127.6	468 F g <sup>-1</sup> at 1 A g <sup>-1</sup>	84.3% after 100,000 cycles at 100 A g <sup>-1</sup>	[105]
RPC-2	Mg <sub>2</sub> Al <sub>1</sub> BTC	1035	434 F g <sup>-1</sup> at 1 A g <sup>-1</sup>	96% after 100,000 cycles at 100 A g <sup>-1</sup>	[106]
LHPC-900	sodium lignosulfonate	2460	298 F g <sup>-1</sup> at 0.1 A g <sup>-1</sup>	97% after 8000 cycles at 2 A g <sup>-1</sup>	[108]
BC-SP-1	shrimp shells	1194.2	311.45 F g <sup>-1</sup> at 0.5 A g <sup>-1</sup>	87.5% after 5000 cycles at 10 A g <sup>-1</sup>	[109]
SSC-700	soybean straw	2012.6	380.5 F g <sup>-1</sup> at 0.5 A g <sup>-1</sup>	73.97% after 10,000 cycles at 10 A g <sup>-1</sup>	[110]
BAPC-800	mantis shrimp shells	2951	401 F g <sup>-1</sup> at 0.5 A g <sup>-1</sup>	97.3% after 10,000 cycles at 5 A g <sup>-1</sup>	[111]
ST-SBC <sub>3</sub>	bagasse	1351.7	418.5 F g <sup>-1</sup> at 0.5 A g <sup>-1</sup>	98.9% after 10,000 cycles at 2 A g <sup>-1</sup>	[112]
GPC-4	garlic shoots	2776	663.1 F g <sup>-1</sup> at 0.5 A g <sup>-1</sup>	97.2% after 8000 cycles at 10 A g <sup>-1</sup>	[113]
APHM150	pine wood	2985.6	339.8 F g <sup>-1</sup> at 0.5 A g <sup>-1</sup>	98.0% after 10,000 cycles at 5 A g <sup>-1</sup>	[114]

internal template. The approach involves an initial low-temperature carbonization step to fix the native channel structure, followed by a high-temperature activation/carbonization step to generate hierarchical porosity within the tube walls, thereby realizing a synergistic combination of natural architecture and activation-induced pores. The obtained sample, ST-SBC<sub>3</sub>, exhibited a high BET surface area (1351.7 m<sup>2</sup> g<sup>-1</sup>). When employed as electrode material in a symmetric supercapacitor (two-electrode configuration), the porous carbon delivered an ultrahigh specific capacitance of 418.5 F g<sup>-1</sup> at 0.5 A g<sup>-1</sup> and retained ≈98.9% of its capacity after 10,000 cycles at 2 A g<sup>-1</sup><sup>[112]</sup>. Liu et al. reported a facile one-step carbonization and activation method to convert garlic shoots biomass into *in situ* N-doped hierarchical porous carbon (GPCs). After optimization, GPC-4 exhibited an ultrahigh BET surface area of 2776 m<sup>2</sup> g<sup>-1</sup> and delivered an exceptionally high specific capacitance of 663.1 F g<sup>-1</sup> at 0.5 A g<sup>-1</sup>. The material also demonstrated excellent cycling stability, retaining ≈97.2% of its initial capacitance after 8000 cycles at 10 A g<sup>-1</sup>, indicating that the one-step route simultaneously achieves high surface area, superior electrochemical performance, and scalable production potential<sup>[113]</sup> (Figure 14). Lu et al. proposed and validated a one-step improved route consisting of hydrothermal modification, carbonization and activation to enhance the pore architecture and specific surface area of biomass-derived porous carbons using pine wood as the precursor. Hydrothermal modification disrupts the crosslinked structure of the biomass and partially removes hemicellulose, which significantly increases the specific surface area of the resulting biochar and enables the subsequent carbonization and activation step to produce a more highly developed pore network. The optimized sample APHM150 exhibited a BET surface area as high as 2985.6 m<sup>2</sup> g<sup>-1</sup> and delivered a specific capacitance of 339.8 F g<sup>-1</sup> at 0.5 A g<sup>-1</sup> in three-electrode tests. A symmetric device assembled with this material in an aqueous electrolyte demonstrated excellent retention, maintaining 98.0% of its capacitance after 10,000 cycles at 5 A g<sup>-1</sup>. The authors highlight that tuning the biochar's specific surface area is a key determinant of the final porous carbon's textural properties and electrochemical performance, and that this method provides a valuable approach for preparing high-surface-area biomass-derived carbons.<sup>[114]</sup>

#### 4. Summary and Outlook

This review has systematically summarized and compared the advances and underlying mechanisms of the three main templating strategies, including hard templates, soft templates, and self-templates, for the synthesis of porous carbon electrodes used in supercapacitors. Representative examples of materials prepared by different templating routes, along with their templates, surface areas, specific capacitances, and cycling performances, are compiled in Table 1 to facilitate cross-comparison and serve as design references.

Overall, templating methods offer a versatile and powerful platform for constructing high-performance porous carbon electrodes. Their foremost advantage lies in the exceptional control

they provide over the hierarchical pore structure; by selecting templates with defined sizes and morphologies, the pore-size distribution, channel geometry, and synergy between different pore classes can be precisely engineered, which is crucial for optimizing ion transport and charge storage. Beyond structural control, these methods facilitate the simultaneous tuning of chemical composition and surface properties. The strategic use of heteroatom-doped precursors or templates enables the seamless incorporation of elements like nitrogen or sulfur, which enhances pseudocapacitance, improves wettability, and boosts electronic conductivity. Furthermore, the very nature of the templating process, where the pore architecture is replicated from a predefined structure, provides a more reliable and reproducible pathway for material synthesis compared to nontemplated methods. This inherent controllability and consistency represent a significant advantage for scaling up production and bridging the gap between laboratory research and industrial manufacturing.

Despite their considerable promise, mainstream templating strategies are hampered by several critical challenges. A primary concern is economic viability, as the synthesis of specialized templates and the multistep fabrication process incur high material and energy costs. Furthermore, the removal of most templates relies on hazardous etching agents, creating operational risks and generating harmful waste streams that pose significant environmental burdens. The structural integrity of the carbon framework is also at risk, with potential pore collapse during high-temperature treatment or etching compromising the designed architecture. Most critically, a substantial gap persists between laboratory proof-of-concept and viable industrial manufacturing. Scaling up introduces profound challenges in maintaining structural uniformity and process control across large volumes. The complexity of multistep synthesis, combined with the difficulty in achieving homogeneous template dispersion and complete removal at scale, severely impacts production yield, cost-effectiveness, and the reproducibility required for commercial application.

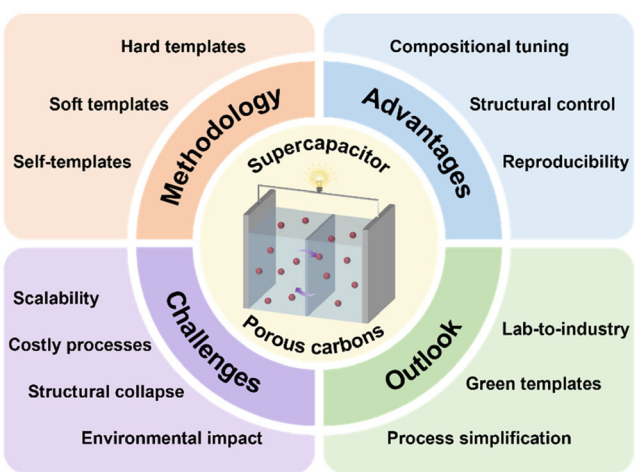


Figure 15. Key aspects of templating strategies for porous carbon electrodes, covering methodology, advantages, challenges, and outlook.

To overcome these barriers, future efforts should prioritize the development of green templating strategies that are inherently scalable and environmentally sound. Promising pathways include ice-templating via freeze-drying, which creates macroporous networks without chemical residues, and the use of soluble salts like NaCl or KCl, which can be removed by simple water washing and recycled. Similarly, leveraging waste biomass (e.g., eggshells, shrimp shells) or natural minerals provides cost-effective and sustainable routes to hierarchically porous carbons. Critically, the focus must extend beyond laboratory material synthesis to address the key challenges of industrial translation. This entails simplifying multistep processes, ensuring batch-to-batch consistency with standardized templates, and conducting rigorous techno-economic analyses to bridge the gap between promising electrochemistry and viable large-scale manufacturing (Figure 15).

## Acknowledgements

The authors are grateful for the financial support provided by the Sichuan Provincial Science and Technology Support Program (2025ZNSFSC0966) and the College Students' Innovative Entrepreneurial Training Plan Program of Sichuan University (202510610110).

## Conflict of Interest

The authors declare no conflict of interest.

**Keywords:** aqueous energy storage · electrodes · porous carbon · supercapacitors · template method

- [1] C. Zhang, L. Hou, W. Yang, S. Du, B. Jiang, H. Bai, Z. Li, C. Wang, F. Yang, Y. Li, *Chem. Eng. J.* **2023**, *467*, 143410.
- [2] Q. Lv, Z. Tian, W. Li, G. Duan, X. Han, C. Zhang, S. He, H. Mao, C. Ma, S. Jiang, *Chin. Chem. Lett.* **2025**, 110860. <https://doi.org/10.1016/j.clet.2025.110860>.
- [3] Z. Shang, X. An, S. Nie, N. Li, H. Cao, Z. Cheng, H. Liu, Y. Ni, L. Liu, *J. Bioresour. Bioprod.* **2023**, *8*, 292.
- [4] Z. Tian, Z. Guo, G. Duan, J. Han, W. Li, Y. Huang, X. Han, C. Zhang, S. He, H. Hou, S. Jiang, *Adv. Fiber Mater.* **2025**, <https://doi.org/10.1007/s42765-025-00584-z>.
- [5] Z. Tian, Z. Guo, G. Duan, Y. Huang, W. Li, X. Han, C. Zhang, S. He, H. Mao, S. Jiang, *Energy Storage Mater.* **2025**, *79*, 104347.
- [6] Y. Liu, K. Xiang, W. Zhou, W. Deng, H. Zhu, H. Chen, *Small* **2024**, *20*, 2308741.
- [7] S. Zeng, G. Duan, R. Yu, Q. Qin, S. He, S. Jiang, H. Yang, X. Han, J. Han, B. Y. Xia, *Prog. Mater. Sci.* **2025**, *147*, 101356.
- [8] T. Guo, L.-B. Tang, W.-N. Deng, G.-D. Liu, W. Zhou, H. Wan, L.-C. Meng, H. Chen, *Rare Met.* **2025**, *44*, 4631.
- [9] X.-Y. Wen, W. Li, H. Chen, W. Zhou, K.-X. Xiang, *Rare Met.* **2025**, *44*, 3881.
- [10] A. C. M. Loy, S. Bhattacharya, *J. Bioresour. Bioprod.* **2024**, *9*, 127.
- [11] Y. Zhang, H. Fang, L. Guan, Y. Li, Y. Yao, Y. Wan, D. Kong, M. Huang, W. Wang, B. Wang, N. Wang, D. Zhang, Y. Li, M. Wu, *J. Power Sources* **2024**, *593*, 233966.
- [12] W. Zhang, T. Xia, X. Huo, X. Li, S. Park, L. Lin, G. Diao, Y. Piao, *J. Electroanal. Chem.* **2022**, *920*, 116615.

- [13] F. Li, M. Huang, J. Wang, J. Qu, Y. Li, L. Liu, V. K. Bandari, Y. Hong, B. Sun, M. Zhu, F. Zhu, Y. X. Zhang, O. G. Schmidt, *Energy Storage Mater.* **2020**, *27*, 17.
- [14] Y. Wang, J. Xiao, T. Zhang, L. Ouyang, S. Yuan, *ACS Appl. Mater. Interfaces* **2021**, *13*, 45670.
- [15] Y. Wang, T. Zhang, J. Xiao, X. Tian, S. Yuan, *J. Mater. Sci. Technol.* **2023**, *134*, 142.
- [16] Y. Wang, T. Zhang, X. Zheng, X. Tian, S. Yuan, *ACS Appl. Mater. Interfaces* **2023**, *15*, 59413.
- [17] T. Liu, J. Zhang, Z. Zhong, X. Huang, J. Yu, Y. Wang, S. Yuan, *J. Mater. Sci.* **2025**, *60*, 1952.
- [18] Y. Yang, Y. Yang, X. Qi, T. Zeng, Y. Wang, S. Yuan, *J. Electroanal. Chem.* **2024**, *972*, 118610.
- [19] M. E. Guye, M. D. Dabaro, H. Kim, *J. Energy Storage* **2025**, *115*, 116037.
- [20] Y. Chen, Q. Tang, Y. Lei, C. Shen, X. Chen, *Diamond Relat. Mater.* **2024**, *148*, 111412.
- [21] D. Guo, Y. Zhang, G. Du, X. Xie, J. Zhang, *J. Power Sources* **2025**, *649*, 237438.
- [22] M. Yi, V. Budarin, H. Yue, G. Tajuelo-Castilla, E. Morales, G. J. Ellis, P. S. Shuttleworth, *J. Colloid Interface Sci.* **2025**, *700*, 138456.
- [23] J. Yang, J. Peng, Y. Tang, P. Liu, C. Yi, Y. Shen, L. Zheng, X. Wang, *Electrochim. Acta* **2025**, *523*, 145880.
- [24] J. Du, A. Chen, X. Gao, H. Wu, *J. Ind. Eng. Chem.* **2022**, *109*, 486.
- [25] B. Cheng, B. Yang, X. Xie, L. Wan, J. Chen, C. Du, Y. Zhang, M. Xie, *Chem. Eng. J.* **2024**, *499*, 156672.
- [26] F. Liu, C. Zhang, W. Huang, L. Chen, Y. Wang, J. Niu, X. Chuan, *RSC Adv.* **2024**, *14*, 13190.
- [27] C. F. Varela, L. C. Moreno-Aldana, Y. Y. Agámez-Pertuz, *J. Bioresour. Bioprod.* **2024**, *9*, 58.
- [28] M. S. M. Zaini, M. Arshad, S. S. A. Syed-Hassan, *J. Bioresour. Bioprod.* **2023**, *8*, 66.
- [29] L. Hu, Q. Zhu, Q. Wu, D. Li, Z. An, B. Xu, *ACS Sustainable Chem. Eng.* **2018**, *6*, 13949.
- [30] F. Shen, M. Qiu, Y. Hua, X. Qi, *ChemistrySelect* **2018**, *3*, 586.
- [31] X. Zhang, W. Jian, L. Zhao, F. Wen, J. Chen, J. Yin, Y. Qin, K. Lu, W. Zhang, X. Qiu, *Colloids Surf. A* **2022**, *636*, 128191.
- [32] K. S. W. Sing, *Pure Appl. Chem.* **1985**, *57*, 603.
- [33] H. Du, Y. Yang, C. Zhang, Y. Li, J. Wang, K. Zhao, C. Lu, D. Sun, C. Lu, S. Chen, X. Ma, *J. Power Sources* **2024**, *614*, 234988.
- [34] S. M. Benoy, D. Bhattacharjya, M. Bora, B. K. Saikia, *ACS Appl. Electron. Mater.* **2022**, *4*, 6322.
- [35] K. Wang, X. Dong, R. Yan, S. Jia, B. Cui, Q. Zhao, Y. Song, *Electrochim. Acta* **2024**, *504*, 144962.
- [36] Z. Chen, X. Wang, B. Xue, W. Li, Z. Ding, X. Yang, J. Qiu, Z. Wang, *Carbon* **2020**, *161*, 432.
- [37] X. Yang, H. He, T. Lv, J. Qiu, *Mater. Sci. Eng.: R.* **2023**, *154*, 100736.
- [38] C. Yuan, X. Cheng, S. A. El-khodary, M. Chen, B. Cao, G. Ni, S. Zhong, P. Bartocci, S. Wang, *Chem. Eng. J.* **2025**, *516*, 164036.
- [39] B. Jache, C. Neumann, J. Becker, B. M. Smarsly, P. Adelhelm, *J. Mater. Chem.* **2012**, *22*, 10787.
- [40] L. Yu, X. Y. Yu, X. W. Lou, *Adv. Mater.* **2018**, *30*, 1800939.
- [41] X. Wang, J. Feng, Y. Bai, Q. Zhang, Y. Yin, *Chem. Rev.* **2016**, *116*, 10983.
- [42] G. Gu, X. Meng, Y. Xie, W. Wang, J. Wang, C. Liu, J. Li, J. Qiu, *Chem. Eng. Sci.* **2025**, *308*, 121370.
- [43] X. Wang, X. Wang, X. Zhou, X. Yang, X. Wu, P. Zhou, J. Zhou, S. Zhuo, *J. Energy Storage* **2023**, *57*, 106221.
- [44] Y. Lu, Q. Zhang, S. Lei, X. Cui, S. Deng, Y. Yang, *ACS Appl. Energy Mater.* **2019**, *2*, 5591.
- [45] Y. Dou, X. Zhang, G. Chen, X. Jiang, X. Li, L. Yu, *J. Alloys Compd.* **2025**, *1010*, 177107.
- [46] Y. Jiang, Z. He, X. Cui, Z. Liu, J. Wan, Y. Liu, F. Ma, *ACS Appl. Energy Mater.* **2022**, *5*, 15199.
- [47] Y. Wang, Z. Shang, T. Zhang, C. Wu, Y. Dai, S. Yuan, *Nanoscale* **2025**, *17*, 17568.
- [48] Z. Shang, T. Zhang, Q. Yang, D. Wang, Y. Liao, D. Xie, Y. Dai, Y. Wang, S. Yuan, *J. Power Sources* **2025**, *633*, 236468.
- [49] D. Xie, S. Liu, W. Wei, Z. Zhou, X. Fu, Z. Shang, Y. Wang, S. Yuan, *Ind. Eng. Chem. Res.* **2024**, *63*, 21146.
- [50] H. Yu, Z. Jiang, Z. Sun, Y. Zhang, H. Deng, L. Yang, Q. Wu, X.-Z. Wang, Z. Hu, *ACS Appl. Energy Mater.* **2025**, *8*, 7330.
- [51] Q. Zhang, D. Sun, K. Wang, Z. Ma, T. Xiao, J. Gao, C. Xu, Z. Xiao, X. Ma, *J. Colloid Interface Sci.* **2025**, *679*, 1219.
- [52] T. Song, Y. Zhao, C. Chen, X. Gui, X. Wu, X. Wang, *J. Energy Storage* **2024**, *98*, 113148.

- [53] J.-O. Jang, S.-Y. Kang, J.-M. Yun, B.-M. Lee, J.-H. Choi, *Sustainable Mater. Technol.* **2025**, *45*, e01501.
- [54] Y. Tong, C. Wu, H. He, Y. Wang, S. Yuan, *J. Power Sources* **2025**, *644*, 237086.
- [55] Y. Hou, Q. Sun, H. Du, *J. Alloys Compd.* **2023**, *937*, 168399.
- [56] X. Yang, G. Sun, F. Wang, L. Chen, Z. Zhang, Y. Zhen, D. Wang, F. Fu, R. a. Chi, *Fuel* **2024**, *366*, 131367.
- [57] J. Li, X. Xie, W. Zhong, Z. Liu, W. Jiang, G. Hu, *Diamond Relat. Mater.* **2024**, *142*, 110856.
- [58] G. Jin, Q. Zhou, Z. Duan, K. Shen, Z. Dong, S. Deng, P. Yang, *ACS Omega* **2024**, *9*, 47557.
- [59] Y. Wang, S. Wu, S. Chang, K. Rong, S. Dong, *ACS Appl. Mater. Interfaces* **2025**, <https://doi.org/10.1021/acsmi.5c10539>.
- [60] X. Fan, W. Zhang, Y. Xu, J. Zheng, Y. Li, X. Fan, F. Zhang, J. Ji, W. Peng, *J. Colloid Interface Sci.* **2022**, *624*, 51.
- [61] S. K. Das, L. Pradhan, B. K. Jena, S. Basu, *Carbon* **2023**, *201*, 49.
- [62] L. Tong, T. Wang, Y. Chen, G. Lin, L. He, X. Liu, *Diamond Relat. Mater.* **2023**, *134*, 109787.
- [63] S. Wang, L. Li, H. Wang, X. Wang, T. Wang, *ACS Appl. Energy Mater.* **2024**, *7*, 4268.
- [64] S. Zhu, N. Zhao, J. Li, X. Deng, J. Sha, C. He, *Nano Today* **2019**, *29*, 100796.
- [65] D. He, Y. Gao, Z. Wang, Y. Yao, L. Wu, J. Zhang, Z.-H. Huang, M.-X. Wang, *J. Colloid Interface Sci.* **2021**, *581*, 238.
- [66] H. Zhang, Y. Song, Y. Liu, J. Zhao, Y. Li, *Electrochim. Acta* **2022**, *431*, 141131.
- [67] H. Wang, Y. Cai, Z. Zhang, Y. Liu, R. Zhang, R. Huo, R. Wu, H. Cheng, J. Yin, J. Yin, Z. Su, H. Zhu, *J. Energy Storage* **2025**, *110*, 115329.
- [68] X. Ni, Y. Zhao, P. Cai, Q. Xu, D. Li, *Diamond Relat. Mater.* **2024**, *148*, 111451.
- [69] X. Zhang, Z. Yu, X. Ma, W. Yue, J. Li, Y. Zhang, *J. Ind. Eng. Chem.* **2025**, *143*, 368.
- [70] Y. Xi, Z. Xiao, H. Lv, H. Sun, X. Wang, Z. Zhao, S. Zhai, Q. An, *Diamond Relat. Mater.* **2022**, *128*, 109219.
- [71] Y. Tian, X. Zhu, M. Abbas, D. W. Tague, M. A. Wunch, J. P. Ferraris, K. J. Balkus, *ACS Appl. Energy Mater.* **2022**, *5*, 6805.
- [72] F. Fu, D. Yang, Y. Fan, X. Qiu, J. Huang, Z. Li, W. Zhang, *J. Colloid Interface Sci.* **2022**, *628*, 90.
- [73] H. Li, Y. Li, Y. Li, H. Shen, S. Zhu, Y. Zhu, K. Lian, *J. Energy Storage* **2024**, *77*, 110000.
- [74] Y. Lin, F. Li, X. Li, H. Zhao, G. Liu, *ACS Appl. Energy Mater.* **2023**, *6*, 2265.
- [75] J. Wang, Z. Sun, S. Wu, X. You, C. Yang, M. Xiong, Z. Li, J. Chen, Y. Liu, F. Guo, *Biomass Bioenergy* **2025**, *200*, 108021.
- [76] S. Wang, J. Feng, H. Pan, *Colloids Surf. A* **2022**, *651*, 129622.
- [77] X. Hou, P. Ren, W. Tian, R. Xue, B. Fan, F. Ren, Y. Jin, *J. Power Sources* **2024**, *603*, 234408.
- [78] J. Liu, X.-W. Mei, F. Peng, *Chin. Chem. Lett.* **2023**, *34*, 108187.
- [79] B. Chen, Z. Qi, B. Chen, X. Liu, H. Li, X. Han, G. Zhou, W. Hu, N. Zhao, C. He, *Angew. Chem. Int. Ed.* **2024**, *63*, e202316116.
- [80] A. Gao, N. Guo, M. Yan, M. Li, F. Wang, R. Yang, *Microporous Mesoporous Mater.* **2018**, *260*, 172.
- [81] L. Feng, H. Liu, W. Zan, S. Li, Y. Chang, Y. Zhang, W. Hou, Y. Zhao, S. Zhu, G. Han, *Chem. Eng. J.* **2024**, *486*, 150346.
- [82] P. Wang, S. Sun, S. Zhao, X. Cao, S. Sun, *Ind. Crops Prod.* **2023**, *191*, 115952.
- [83] W. Li, T. Wang, J. Guo, P. Liu, X. Yin, D. Wu, *Appl. Surf. Sci.* **2022**, *599*, 153885.
- [84] B. Liang, L. Chen, J. Lv, Y. Li, W. Tan, W. Zhu, J. Hu, K. Zeng, G. Yang, *ACS Appl. Energy Mater.* **2022**, *5*, 6163.
- [85] B. Xue, J. Xu, R. Xiao, *Chem. Eng. J.* **2023**, *454*, 140192.
- [86] X. Hou, P. Ren, W. Tian, B. Fan, T. Wu, J. Wang, Z. Duan, Z. Chen, Y. Jin, *J. Anal. Appl. Pyrolysis* **2025**, *186*, 106934.
- [87] X. Yang, F. Wang, X. Li, Z. Zhang, C. Wang, C. Yang, Y. Zhen, D. Wang, F. Fu, R. a. Chi, *J. Alloys Compd.* **2022**, *921*, 166127.
- [88] Q. Yin, X. Li, X. Yong, P. Sha, Q. Zhang, H. Dong, J. Sui, J. Yu, L. Yu, L. Dong, *Diamond Relat. Mater.* **2023**, *134*, 109798.
- [89] Y. Zhang, X. Ma, Z. Yu, W. Yue, X. Zhang, T. He, *J. Anal. Appl. Pyrolysis* **2024**, *178*, 106411.
- [90] Z. Li, Y. Li, Y. Tian, J. Xiao, F. Pan, S. Liu, *J. Mater. Chem. A* **2025**, *13*, 26534.
- [91] Y. Liang, Y. Yu, X. Qi, *Int. J. Biol. Macromol.* **2025**, *307*, 141938.
- [92] C. Song, H. Lin, T. Wang, B. Li, R. Lu, S. Zhang, *Energy Fuels* **2023**, *37*, 7511.
- [93] J. Wang, C. Zhang, Z. Chen, J. Dong, P. Chang, T. Yang, J. Zhang, P.-Y. Zhao, *Diamond Relat. Mater.* **2024**, *149*, 111587.
- [94] Z. Wu, K. Zhang, C. Ma, S. Luo, W. Li, S. Liu, *J. Energy Storage* **2023**, *68*, 107619.
- [95] Y. Zhao, B. Huang, Y. Ji, Y. Yu, X. Gao, Z. Zhang, H.-F. Fei, *ACS Appl. Mater. Interfaces* **2023**, *15*, 5644.
- [96] R. Wang, L. Chen, Y. Wen, Q. Zheng, D. Jiao, L. Yue, H. Lv, Y. Yang, S. Luo, Y. Yang, *Ind. Crops Prod.* **2023**, *204*, 117301.
- [97] C. Chen, T. Ren, S. Wu, X. Xin, B. Ge, S. Hao, M. Ma, J. Pang, J. Zhang, *J. Energy Storage* **2024**, *102*, 114192.
- [98] M. Muddasar, M. Mushtaq, A. Beaucamp, T. Kennedy, M. Culebras, M. N. Collins, *ACS Sustainable Chem. Eng.* **2024**, *12*, 2352.
- [99] Y. Zhao, A. Wang, L. Shen, L. Xiao, L. Hou, *Microporous Mesoporous Mater.* **2022**, *341*, 112039.
- [100] Y. Zhao, A. Wang, L. Shen, Z. Zhao, L. Xiao, L. Hou, *J. Appl. Polym. Sci.* **2022**, *139*, e52417.
- [101] Y. Zhao, J. Zhang, Z. Zhao, H. Chen, L. Xiao, L. Hou, *Microporous Mesoporous Mater.* **2022**, *330*, 111614.
- [102] L. Zou, C.-C. Hou, Q. Wang, Y.-S. Wei, Z. Liu, J.-S. Qin, H. Pang, Q. Xu, *Angew. Chem. Int. Ed.* **2020**, *59*, 19627.
- [103] T. K. Ghosh, D. L. Singh, G. R. Rao, *Electrochim. Acta* **2024**, *500*, 144752.
- [104] X. Gang, M. Krishnamoorthy, W. Jiang, J. Pan, Z. Pan, X. Liu, *Carbon* **2021**, *171*, 62.
- [105] U. A. Kolachi, N. H. Solangi, Y. Sun, R. Andavar, I. Shahid, J. Zhao, J. Pan, *J. Mater. Chem. A* **2025**, *13*, 22142.
- [106] N. Jiang, Y. Sun, J. Pan, *J. Colloid Interface Sci.* **2026**, *702*, 138908.
- [107] J. Pang, W. Zhang, J. Zhang, G. Cao, M. Han, Y. Yang, *Green Chem.* **2017**, *19*, 3916.
- [108] L. Zhao, W. Jian, X. Zhang, F. Wen, J. Zhu, S. Huang, J. Yin, K. Lu, M. Zhou, W. Zhang, X. Qiu, *J. Energy Storage* **2022**, *53*, 105095.
- [109] W. Yue, Z. Yu, X. Zhang, H. Liu, J. Li, Y. Zhang, X. Ma, *Appl. Surf. Sci.* **2025**, *685*, 162100.
- [110] S. Jiao, L. Zhang, C. Li, H. Zhang, J. Zhang, P. Li, Y. Tao, X. Zhao, H. Chen, J. Jiang, *Ind. Crops Prod.* **2022**, *183*, 114906.
- [111] Y. Sun, D. Xu, Z. He, Z. Zhang, L. Fan, S. Wang, *J. Mater. Chem. A* **2023**, *11*, 20011.
- [112] M. Xu, A. Wang, Y. Xiang, A. Ejaz, J. Niu, *Ind. Crops Prod.* **2022**, *176*, 114291.
- [113] F. Liu, J. Liu, J. He, J. Niu, P. Feng, X. Chuan, *J. Energy Storage* **2025**, *134*, 118210.
- [114] Y. Lu, G. Zhou, Z. Zhang, C. Li, Q. Dong, Y. Su, W. Chen, *Chem. Eng. J.* **2025**, *508*, 161085.

Manuscript received: August 28, 2025

Revised manuscript received: September 30, 2025

Version of record online: